8-2022

Synthesis of Modular DO3A-Based High-Relaxivity Contrast Agents for MRI of Prostate Cancer

Dana Qiang Murphy Soika
dqm8699@rit.edu

Synthesis of Modular DO3A-Based High-Relaxivity Contrast Agents for MRI of Prostate Cancer

Dana Qiang Murphy Soika

A thesis submitted in partial fulfillment of the requirements for the degree

Master of Science in Chemistry

Supervised by

Dr. Hans Schmitthenner

School of Chemistry and Materials Science

College of Science

Rochester Institute of Technology

August 2022

Signature of the Author _____

Accepted by _____

Director, M.S. Degree Program Date

SCHOOL OF CHEMISTRY AND MATERIALS SCIENCE
COLLEGE OF SCIENCE
ROCHESTER INSTITUTE OF TECHNOLOGY
ROCHESTER, NEW YORK

CERTIFICATE OF APPROVAL

M.S. DEGREE THESIS

The M.S. Degree Thesis of Dana Soika has
been examined and approved by the thesis
committee as satisfactory for the thesis required
for the M.S. Degree in Chemistry.

_____
Dr. Hans Schmitthenner, Thesis Advisor

_____
Dr. Christina Goudreau

_____
Dr. Joseph Hornak

_____
Dr. Maureen Ferran

_____
Date

I am dedicating this thesis to my beloved family, for their love, support, and wisdom has and will continue to help me grow into the person I am proud to be today.

To my sister: Jamie Q. M. Soika, a remarkably gifted writer and artist whose support means the world to me. Thank you for always being by my side and cheering me on.

To my aunt: Lou Ann Soika, one of the strongest women I know and lifelong role model. You taught me how to look within myself to find my own empowerment, but also led by example and showed me what it means to be an independent and respected woman in today's world.

And finally, to my moms: to Clementina M. Soika, who taught me the importance of believing in myself, and showed me the value of hard work and dedication in the attainment of my ambitions in life; and to Debra J. Murphy, whose unconditional love and support taught me that even in my darkest moments, I am still worthy of being loved.

You are my sunshine

Acknowledgements

The work detailed in this thesis would not have been possible without the support and encouragement of many. Firstly, I would like to thank my research advisor, Dr. Hans Schmitthenner, for his mentorship and guidance throughout not just my graduate education, but also during my time as an undergraduate student. He believed in me when I stopped believing in myself, and for that I am truly grateful.

I would like to acknowledge the other students in the Molecular Imaging Laboratory, as I've been able to work with many amazing people and learn so much alongside them. In particular, I would like to thank Kels Jones, a previous member of the Molecular Imaging Laboratory, for mentoring me during my first semester as a lab member. Much of what I learned from them provided me with the foundation to take on this High Relaxivity project. Additionally, I would like to thank Andrew O'Brien for his diligent help in running the T_1 relaxivity experiments, as well as previous lab member Damien Dobson for synthesizing the DCL-DSS targeting group I used in my synthesis.

I would like to thank the School of Chemistry and Materials Science at the RIT College of Science for their financial support during my graduate career, as well as the National Institutes of Health and grant that funded both me and this project, thus enabling me to focus on my studies.

I am immensely grateful to my moms, Debra Murphy and Tina Soika, for their lifelong support. Without them, I would not be where I am today. I feel incredibly fortunate to have such selfless parents who have gone through so much to raise and support me throughout my life.

Abstract

Contrast agents (CAs) are small molecules used in magnetic resonance imaging (MRI) to help diagnose various forms of cancer. While MRI is advantageous over other clinical imaging techniques, limitations of today's contrast agents containing gadolinium (Gd) hinder their safety, sensitivity, and specificity. The conventional CAs that MRI relies on are considered low-relaxivity and are not optimally effective at enhancing MR signal. Additionally, they lack cell-specificity and circulate throughout the body. Furthermore, unbound Gd^{3+} is nephrogenic which prevents its use in patients with impaired renal function. In the clinic, these limitations mean high dosages of these compounds must be administered to patients in order to produce an image that struggles to highlight the exact tumor location. Our aim was to improve conventional CAs by synthesizing a high-relaxivity (HR) targeted contrast agent (HR-TCA). The cell-specific nature of the HR-TCA will allow for its accumulation at tumor sites while the HR will produce a stronger MR signal per molecule of CA. Combined, this means a much lower and therefore safer dose of CA can be used to produce an image of the exact tumor location with superior contrast. Our modular approach allows us to easily combine this HR contrast agent (HR-CA) to any targeting peptide using a linker in a convergent, one-step synthesis. Our synthetic approach for the HR-CA module attaches a macrocyclic chelator, DO3A, to the side chain of an orthogonally protected alanine. This is a modification to the approach published by Boros in which t-butyl groups were utilized to protect DO3A. In our modular approach, Gd is chelated early to protect the acetic acid donor arms of DO3A from participating in unwanted side reactions for the remainder of the synthesis, eliminating any need to expose the final HR-TCA to the harsh acidic conditions of TFA that are necessary to remove t-butyl protecting groups. Upon removal of the N- and C-terminal protecting groups, the HR-CA module is coupled directly to our in-house synthesized targeting module which is comprised of the targeting agent (DCL) and linker (DSS) already attached to afford the final HR-TCA. T_1 relaxation measurements of relevant intermediates and the final product were performed to compare their relaxivities with those of commercial CAs used in clinics, labs, and hospitals today. Although the HR-CA and final HR-TCA exhibited only a modest increase in T_1 relaxivity compared to commercial CA Gd-DOTA, in a striking discovery it was observed that the presence of both a tryptophan spacer and an Fmoc protecting group boosted the T_1 relaxivity significantly.

Abbreviations

Frequently Used Solvents

ACN	Acetonitrile
AmAc	Ammonium Acetate
DCM	Dichloromethane
DiH_2O	Deionized Water, 18mΩ
DMF	Dimethylformamide
DMSO	Dimethyl Sulfoxide
EtOAc	Ethyl Acetate
MeOH	Methanol

Frequently Used Reagents and Compounds

Ala	Alanine, a natural amino acid
DCL	N-[N-[(S)-1,3-dicarboxypropyl]carbamoyl]-(S)-L-lysine
DCL	Dichloromethane
DEA	Diethylamine
DIPEA	Diisopropylethylamine
DO3A	1,4,7,10-tetraazacyclododecane-1,4,7-tris(tert-butyl acetate)
DOTA	1,4,7,10-tetraazacyclododecane-1,4,7,10-tetraacetic acid
dTrp	The unnatural isomer of tryptophan
Ms-Cl	Methane Sulfonyl Chloride
Ser	Serine, a natural amino acid
TEA	Triethylamine
TFA	Trifluoroacetic Acid
Trp	Tryptophan, a natural amino acid

Instrumentation

HPLC-MS	High-Pressure Liquid Chromatography Mass Spectrometry
HRMS	High Resolution Mass Spectrometry
LR-MS	Low Resolution Mass Spectrometry

NMR	Nuclear Magnetic Resonance
SPE	Solid Phase Extraction
SPPS	Solid Phase Peptide Synthesis

Molecular Imaging Terms

CA	Contrast Agent
CFM	Confocal Microscopy
HR-CA	High-Relaxivity Contrast Agent
HR-TCA	High-Relaxivity Targeted Contrast Agent
MRI	Magnetic Resonance Imaging
TCA	Targeted Contrast Agent
TMIA	Targeted Molecular Imaging Agent

Table of Contents

Acknowledgements ---- iv
Abstract ---- v
Abbreviations ---- vi
Table of Contents ---- viii
List of Figures ---- x
List of Schemes ---- xi
List of Tables ---- xi
Introduction ---- 1
Background: Cancer ---- 1
Molecular Imaging and MRI in Cancer Treatment ---- 2
Biomarkers and Receptors: Molecular Targeting ---- 3
Prostate-Specific Membrane Antigen Receptor ---- 4
Domains, Active Site, and Mechanism of PSMA ---- 5
Targeting PCa with DCL ---- 6
Significance of PSMA ---- 8
Background: Magnetic Resonance Imaging ---- 9
MRI Scanners ---- 9
T_1 and T_2 Relaxation ---- 11
Contrast Agents and Their Limitations ---- 13
Synthetic Approach ---- 17
Modular Approach to TMIA Synthesis ---- 17
Synthetic Approach to High Relaxivity Contrast Agents ---- 18
Novel Use of Metals as DO3A Protecting Groups ---- 18
Evaluation and Analysis of Compounds ---- 19
Results and Discussion ---- 19
Use of Tryptophan as a Spacer ---- 22
The Struggle of Optimizing the tert-Butyl Deprotection with TFA ---- 25
To use buffered solution, or not to use buffered solution? ---- 30
Relaxivity Measurements ---- 31
Conclusions ---- 34
Experimental Procedures ---- 35
General Considerations ---- 35
Cbz-Ser(Ms)-OBn (2) ---- 35

Cbz-Ala(Cyclen)-OBn (3) ---- 36
Cbz-Ala(DO3A-tBu3)-OBn (4) ---- 36
Cbz-Ala(DO3A)-OBn (5) ---- 36
Cbz-Ala(Gd-DO3A)-OBn (6) ---- 37
H-Ala(Gd-DO3A)-OH (7) ---- 37
Fmoc-Trp-Ala(Gd-DO3A)-OH (8) ---- 37
H-Trp-Ala(Gd-DO3A)-OH (9) ---- 38
DCL-DSS-Trp-Ala(Gd-DO3A)-OH (10) ---- 38
Appendix I – HPLC-MS and HRMS Data ---- 39
Compound 4: Cbz-Ala(DO3A-tBu3)-OBn ---- 39
Compound 5: Cbz-Ala(DO3A)-OBn ---- 39
Compound 6: Cbz-Ala(Gd-DO3A)-OBn ---- 40
Compound 7: H-Ala(Gd-DO3A)-OH ---- 43
Compound 8: Fmoc-dTrp-Ala(Gd-DO3A)-OH ---- 45
Compound 9: H-dTrp-Ala(Gd-DO3A)-OH ---- 47
Compound 10: DCL-DSS-dTrp-Ala(Gd-DO3A)-OH ---- 48
DSS-Trp-Ala(Gd-DO3A)-OH ---- 51
T_1 Relaxivity Data ---- 53
References ---- 56

List of Figures

Figure 1: Structure of serum albumin targeted contrast agent, Vasovist ---------- 3
Figure 2: The two subunits of PSMA ---------- 4
Figure 3: Hydrolysis of N-acetyl-aspartyl-L-glutamic acid by PSMA. ---------- 5
Figure 4: Domains of PSMA ---------- 5
Figure 5: Active sites of the PSMA receptor ---------- 5
Figure 6: Catalytic mechanism of PSMA ---------- 6
Figure 8: Structure of DCL of compound **10** ---------- 7
Figure 9: Structure of our previously reported DCL-DSS-Lys(Cy5.5) TMIA for CFM ---------- 8
Figure 10: CFM images of previously reported DCL-DSS-Lys(Cy5.5) TMIA in cells ---------- 8
Figure 11: Diagram of a typical MRI instrument and magnetic coils housed inside ---------- 10
Figure 12: Typical free induction decay ---------- 10
Figure 13: T_1 relaxation diagram showing net magnetization vector returning to equilibrium ------- 11
Figure 14: T_2 relaxation diagram showing dephasing of spins in the xy-plane ---------- 11
Figure 15: T_1 relaxivities of some commercial MRI CAs compared to free Gd^{3+} ---------- 12
Figure 16: Diagram of water molecules in the outer and inner coordination spheres of a CA ----- 13
Figure 17: Equation for relaxation rate constant ---------- 13
Figure 18: Equation describing T_1 relaxivity (r_1) ---------- 13
Figure 19: Structures of macrocyclic chelators DOTA, DO3A, and Gd-DO3A ---------- 14
Figure 20: A selection of commonly used commercial aminocarboxylate-based MRI CAs --------- 16
Figure 21: T_1 relaxivities (r_1) of CAs from our previous work compared to Dotarem ---------- 16
Figure 23: Structures of CA modules based on Lysine and Alanine ---------- 18
Figure 24: T-butyl deprotection formation of product, mono- and di-t-butyl intermediates --------- 21
Figure 25: T_1 relaxivities of Gd-DOTA, Fmoc-dTrp-Ala(Gd-DO3A)-OH (**8**), H-dTrp-Ala(Gd-DO3A)-OH (**9**), and DCL-DSS-dTrp-Ala(Gd-DO3A)-OH (**10**) ---------- 32
Figure 26: Third set of T_1 relaxivity data of F-dTrp-Ala(Gd-DO3A)-OH (**8**) ---------- 32

List of Schemes

Scheme 1: General synthetic approach for TMIAs using DCL pre-coupled to DSS linker --------- 17

Scheme 2a: Part 1 of the reaction schematic for the proposed HR-TCA---------- 20

Scheme 2b: Part 2 of the reaction schematic for the entire proposed HR-TCA ---------- 24

Scheme 3: Potential unwanted side reaction caused by TFA and TIPS ---------- 26

Scheme 4: Schematic of basic buffer-dependent side transformation of compound ---------- 30

List of Tables

Table 1. List of selected tert-Butyl deprotection experiments ---------- 29

Introduction

Background: Cancer

Despite breakthroughs in modern medicine such as chemotherapy, radiation therapy, and the development of molecular imaging, cancer persists as one of the leading causes of death worldwide. In 2016, it was the leading cause of death for individuals between the ages of 30 and 69 throughout 50 countries around the world.[1] After heart disease, it was the leading cause of death in 2017 claiming 599,108 lives.[2] According to the CDC, prostate cancer (PCa) is the second leading cause of cancer death in American men. It is estimated that 1 in 8 men will be diagnosed with PCa sometime in their lifetime, and 1 in 41 men will die from it.[3,4] Although our understanding of cancer and cancer treatments are always improving, the number of new global cancer cases per year is expected to reach 23.6 million by 2030.[5] Additionally, the number of US cancer cases is predicted to increase to over 2.2 million, or 49%, by 2050.[6] For these reasons, efforts to develop safer and more effective cancer treatments must continue.

Cancer most often starts localized in a single cell due to an error in a region of DNA called a tumor-suppressor or proto-onco gene. These genes are integral parts of the biological machinery that regulate the cell cycle and cellular growth. While DNA is commonly thought of as the blueprint of life, it also functions as a regulatory system for all the different cellular processes needed to help keep the body healthy. Another way by which cancer can begin is with inappropriate signaling of the proteins and protein complexes that regulate cell growth; Ensuring that these biological processes are properly maintained is critical in preventing the onset and advancement of cancer. Loss of control of the cell cycle can quickly lead to unregulated cell growth and ultimately the start of a tumor.[7-10]

Some types of tumors (such as moles) are harmless, only growing to a certain size and can easily be removed if desired. However, if the tumor is malignant, it can continue growing to the point where it interferes with the body's major organs and hinders their function. Once a malignant tumor has established itself in the body, it can easily catch a ride throughout one of the body's main highways (the lymphatic and circulatory systems) and metastasize. It is for this reason that early detection and treatment are important to improve patient outcomes. If a malignant tumor is not detected in a timely manner, it has a much higher chance of metastasizing and causing more damage than what chemotherapy, radiotherapy, and surgical procedures can treat.[11,12]

Molecular Imaging and MRI in Cancer Treatment

In aggressive cancers that can grow and spread rapidly throughout the body, it is important to obtain a diagnosis as soon as possible. The earlier the tumor is detected, the greater a chance it stays localized and will be easier to remove with surgery or treated with chemotherapy or targeted radiation. There are many non-invasive imaging methods such as x-ray imaging, computed tomography (CT), positron emission tomography (PET), MRI, and ultrasound imaging that can be used by medical professionals for the detection and diagnosis of all kinds of cancers.[13] With any imaging method, the images produced should be of the highest clarity and resolution possible in order to allow physicians to distinguish the boundaries of malignant tumors and their locations within the body. To accomplish this, molecular probes are often used to highlight cancerous cells and better differentiate them from healthy tissue, improving image quality and further assisting in assessing tumor location and metastasis. Unfortunately, detecting cancer in its early stages is often challenging due to the difficulty in distinguishing cancerous cells from healthy tissue.

Detecting cancer, especially in its early stages, is not an easy task. The initial signs of abnormal cell growth preceding the onset of cancer start genetically and primarily affect the tumor microenvironment. This microenvironment is a complex network of tissue and signaling molecules which includes the extracellular matrix, nearby healthy cells, cytokine signaling networks, growth factors, and proteases that control autocrine and paracrine intercellular communication.[14] These initial changes do not always produce a deformation in the body that is readily-observable using current clinical imaging techniques.[15,16] Through changes facilitated by the tumor microenvironment, a cell can gain the ability to evade apoptosis, become insensitive to anti-growth signals, sustain angiogenesis, and replicate indefinitely.[15]

While the cells may start out as a small adenoma, they can remain undetectable to the individual for years but later advance to an observable hyperplasia or dysplasia, an enlargement of a tissue due to abnormally high cell growth and replication. If undetected, these cells become increasingly malignant and the progression of the disease is much more likely to accelerate faster than what chemotherapy and radiation therapy can effectively treat.[12,15] The earlier a tumor is detected, the greater of a chance it is still localized and will be easier to remove with surgery or treated with chemotherapy or targeted radiation.

Biomarkers and Receptors: Molecular Targeting

A multitude of proteins and protein complexes work together nonstop to maintain healthy cell function. They can be localized to the plasma membrane, released outside of the cell for circulation, or exist intracellularly. In diseased cells, the behavior of these proteins, their expression, and even their 3-dimensional structures can deviate significantly from what is considered healthy. Thus, these kinds of changes in a protein or other biomolecule can be associated and correlated with the initiation, progression, and advancement of cancer.

Recent research has sought to improve the effectiveness of CAs by designing them to bind to proteins that are associated either with specific cell types or specific regions of the body. Targeting an imaging agent to a biomarker enables it to accumulate at a specific site in the body which concentrates and increases the signal at the region of interest without making any modifications to the molecular structure of the imaging agent itself. This is a common strategy in molecular imaging that is already used in many imaging applications today. For example, serum albumin, the most abundant blood plasma protein, is present in blood serum at concentrations of 500-700 μM and can be targeted for blood vessel imaging with the contrast agent Vasovist. **(Fig. 1)** Similarly, fibrin can be targeted to image thrombosis and uncontrolled clotting.[13,16]

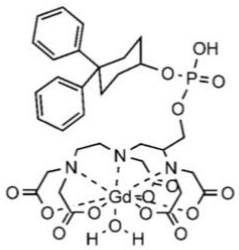

Figure 1: (Above) Structure of serum albumin targeted contrast agent, Vasovist. (Used with permission from Werner et al.)

Different cancers can also have biomarkers that are specific to their particular cell type. For example, breast cancer cells have the potential to overexpress up to three different types of cell membrane receptors: estrogen receptors, progesterone receptors, and human epidermal growth factor 2.[17] Similarly, the discovery of the Prostate-Specific Membrane Antigen (PSMA) as a biomarker provided a means by which PCa could be targeted for improved imaging and monitoring of the disease.

Prostate-Specific Membrane Antigen Receptor

PSMA, also known as Glutamate Carboxypeptidase II (GCPII), is a homodimeric, transmembrane zinc-dependent exopeptidase. In other words, it consists of two monomers (**Fig. 2**) that are anchored into the lipid bilayer of cells, and it uses zinc ions to cleave terminal peptide bonds. Only the extracellular portion of PSMA can be modeled because its transmembrane portion is incompatible with crystallization techniques.[18,19]

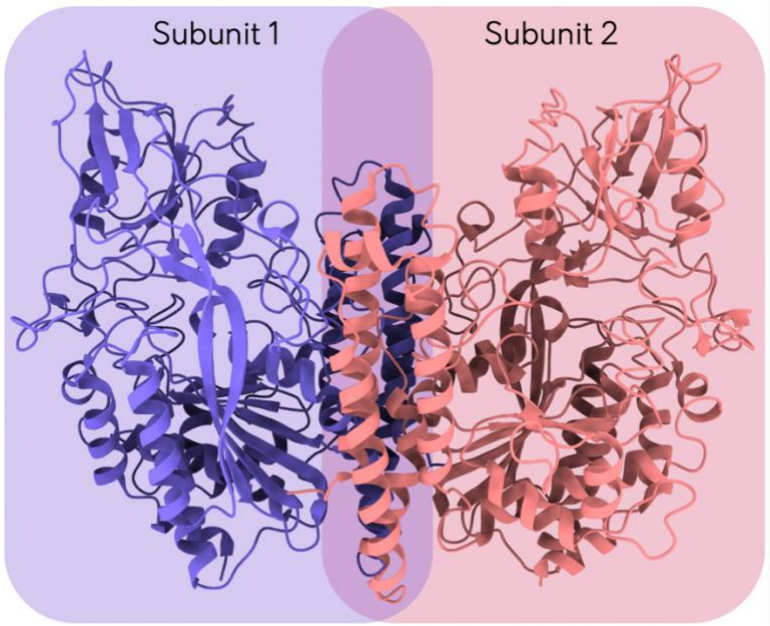

Figure 2: (Above) The two subunits of PSMA. Diagram made in-house. The model of PSMA was imported into molecular visualization program UCSF ChimeraX from the Protein Data Bank (PDB) using PDB ID: 1Z8L. The 3D structure was elucidated by Davis et al. from the X-ray diffraction pattern of crystallized human PSMA.[20] Used with permission.

PSMA can be found in several healthy cell types where its physiological role is tissue dependent. In addition to the secretory acinar epithelium of prostate cells, it can also be found in astrocytes (abundant glial cells of the brain) and Schwann cells (myelin-sheathed cells of the parasympathetic nervous system) where it performs synaptic hydrolysis of N-acetyl-aspartyl-L-glutamic acid (NAAG) to generate the neurotransmitter glutamate.[18,19] (**Fig. 3**) Additionally, it acts as a folate hydrolase in the small intestine to assist the dietary absorption of folate.[21]

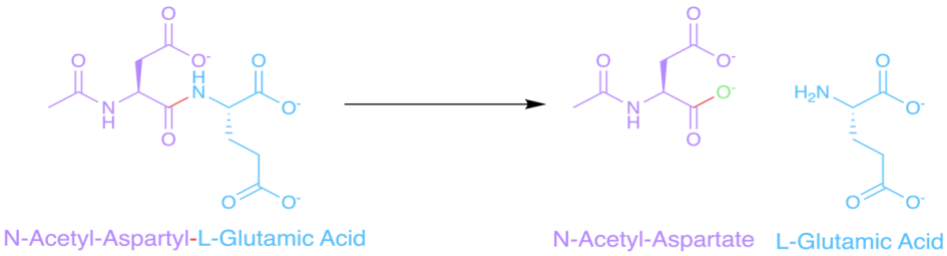

Figure 3: Hydrolysis of N-acetyl-aspartyl-L-glutamic acid by PSMA.

Domains, Active Site, and Mechanism of PSMA

Each subunit of PSMA has three domains: an apical domain, protease domain, and C-terminal domain. (**Fig. 4**) The two dimers are held together by interactions between the C-terminal domain of one monomer, and the apical and protease domains of the other monomer.[19]

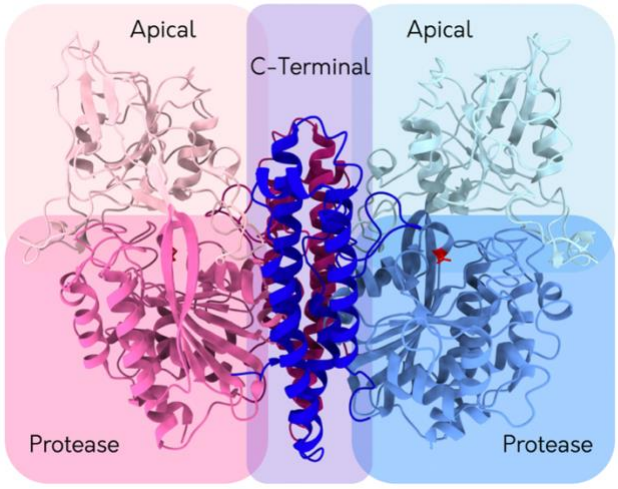

Figure 4: Domains of PSMA. Diagram made in-house. The 3D model of PSMA was imported into molecular visualization program UCSF ChimeraX from PDB ID: 1Z8L. The 3D structure was elucidated by Davis et al. from the X-ray diffraction pattern of crystallized human PSMA. Used with permission.[20]

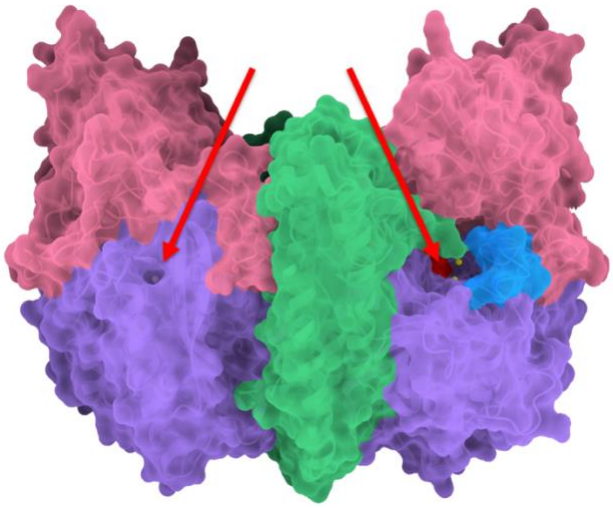

Figure 5: Active sites of the PSMA receptor. Diagram made in-house. The 3D model of PSMA was imported into molecular visualization program UCSF ChimeraX from PDB ID: 1Z8L. The 3D structure was elucidated by Davis et al. from the X-ray diffraction pattern of crystallized human PSMA. Used with permission.[20]

PSMA has two active sites, one in each of its two protease domains, that face in opposite directions. (**Fig. 5**) Inside each active site is a catalytic glutamate that transfers protons between the nucleophile and scissile amide nitrogen, a nucleophile in the form of a hydroxide ion, and two Zn^{2+} ions which help stabilize the transition state of the substrate during the reaction.

The elucidation of the 3D structure of PSMA (and therefore the active site) allowed for the catalytic mechanism to be discovered. (**Fig. 6**) Once the substrate enters and is bound inside the active site, the carbonyl of the peptide bond is polarized through its interactions with the Zn^{2+} ions (circled in red). This induces the hydroxide nucleophile to perform a nucleophilic attack on the amide carbonyl (boxed in orange). The resulting tetrahedral intermediate is then stabilized by the Zn^{2+} ions (boxed in yellow). Finally, the glutamic acid extracts the proton from the hydroxide and shuttles it to the amide nitrogen, causing cleavage of the peptide bond and generating the two products (boxed in green).[18] Understanding this mechanism has enabled the design of inhibitory molecules that can be used to target PSMA. This is a frequently used strategy in molecular imaging: Once a biomarker is found, inhibitors can be designed based on the active site, and the specific binding of the inhibitor to the active site can be used to target cancer.

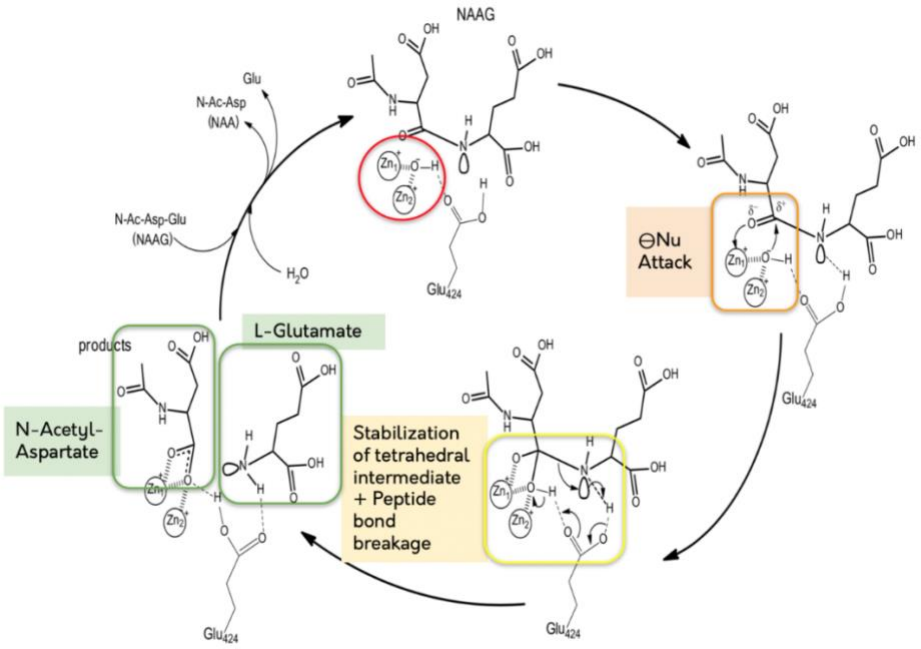

Figure 6: Catalytic mechanism of PSMA.[18] Used with permission from Pavlícek et al.

Targeting PCa with DCL

As an inhibitor with specific binding, DCL can also be used as a targeting group. Inhibitors of PSMA can be classified as either substrate or transition state analogs of NAAG. **Figure 7** shows a comparison between the NAAG substrate (**A**), inhibitors which mimic the peptide bond (**B**), and inhibitors which mimic the transition state of the catalytic mechanism (**C**). The DCL inhibitor (**Fig. 8**) is based on the Glu-Lys dipeptide which mimics the peptide bond. The two residues are joined

together by a urea motif that effectively replaces the peptide bond and prevents its cleavage from taking place.[20,22] PSMA recognizes DCL using its "glutarate sensor", a group of amino acids near the active site consisting of Tyr552, Arg210, and Asn257. In particular, Tyr552 interacts with the α-carboxylic acid (**Fig. 8**, pink) while Arg210 interacts with the γ-carboxylate.[22] (**Fig. 8**, blue)

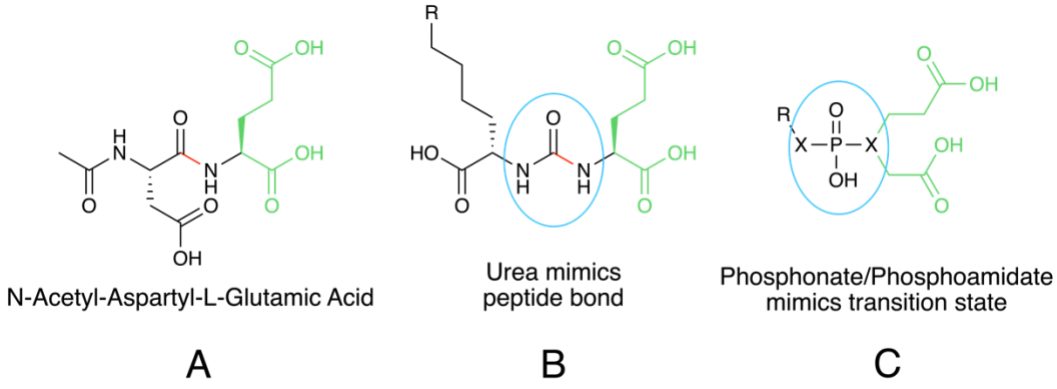

Figure 7: (Above) Structure of NAAG (**A**) compared to structure of PSMA inhibitors that mimic either the peptide bond using a urea motif (**B**), or phosphonate/phosphoamidate that mimics the transition state of the substrate (**C**).

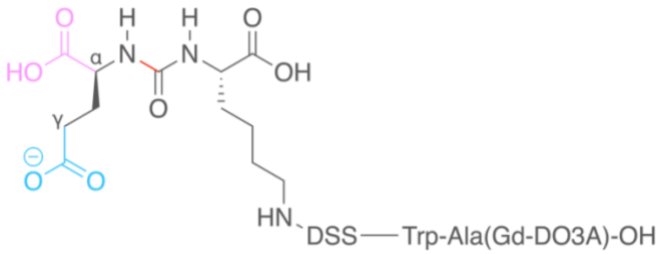

Figure 8: (Above) Structure of DCL of compound **10** with the two portions that PSMA uses for substrate recognition highlighted in pink and blue. The bond that PSMA attempts to cleave is highlighted in red.

While we unfortunately did not have the means to evaluate the relaxivity of these novel compounds *in vivo*, we have previously used confocal microscopy (CFM) to show the efficacy of our targeting group, DCL, to selectively bind to overexpressed PSMA receptors in C42 cells using a near-infrared fluorescent dye, Cy5.5, attached to a lysine side chain. (**Fig. 9**) DCL was shown to have minimal binding to PC3 cells (**Fig. 10**, right) which have normal PSMA expression while overwhelmingly binding to C42 cells (**Fig. 10**, left and middle) which overexpress the PSMA receptor.

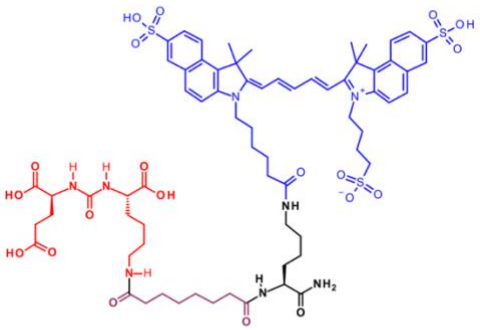

Figure 9: (Above) Structure of our previously reported DCL-DSS-Lys(Cy5.5) TMIA for confocal microscopy (CFM).

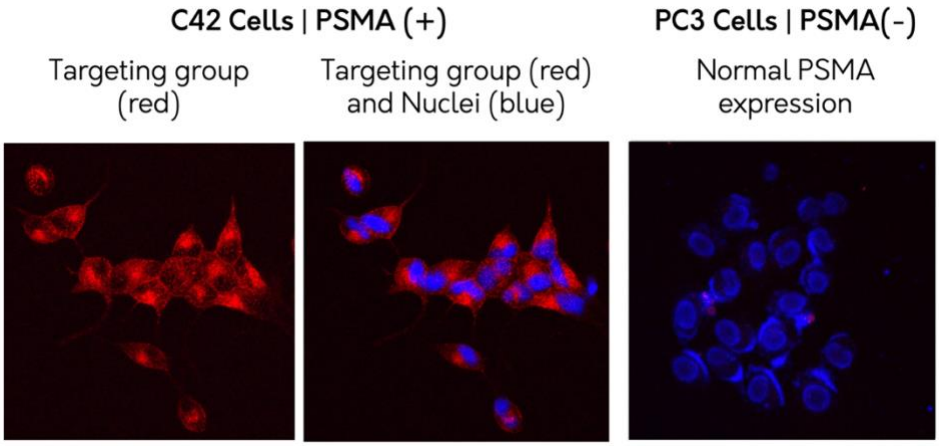

Figure 10: (Above) CFM images of previously reported DCL-DSS-Lys(Cy5.5) TMIA. Images obtained at RIT in Dr. Irene Evans' lab. (Hanafish, A.; Embong, A.; Walden, R.; Anderson, T.; Schmitthenner, H.; Evans, I. (2016, Jan). *Targeted molecular imaging agents (TMIAs) for improved detection of cancers. Molecular Biology of the Cell.*; American Society of Cell Biology (Vol. 27)).

Significance of PSMA

PSMA is heavily involved in the progression of PCa. PCa cells can overexpress PSMA up to 1000-fold compared to healthy cells, enabling for its use as a biomarker. PSMA can also be used as a prognosis indicator, as the amount of overexpression directly correlates with disease progression. High PSMA expression is also associated with a higher risk of recurrence, even after a patient has undergone curative surgery. In addition to its abundance in PCa cells, it can also be found overexpressed in the neovasculature of other solid tumors, thus expanding its potential applications beyond those of just PCa.[22] Even though there are various imaging methods that can be used to image cancerous cells, MRI has many advantages over other modalities.

Background: Magnetic Resonance Imaging

Since its first use in the medical field in the late 1970's, MRI has played a central role in many successful patient outcomes across the globe.[23,24] MRI is advantageous over all other imaging techniques. It can produce much higher resolution images compared to the fuzzy and blurry images of other imaging modalities such as PET. Furthermore, MRI can generate 3D images with sub-millimeter spatial resolution, and its ability to image deep into soft tissues makes it effective in whole-body detection of metastasis. Unlike PET and CT scans, MRI does not require the use of harmful ionizing radiation which can contribute to a patient's overall long-term cumulative radiation exposure which in itself is associated with an increased risk of cancer.[13,16,25] Additionally, MRI is also capable of assessing physiological characteristics such as vascularization, oxygenation, and diffusion.[12,16]

MRI Scanners

MRI is an imaging technique based on nuclear magnetic resonance (NMR) which distinguishes different regions of the body from one another based on differences in the magnetic and physical properties of water in different tissues. All NMR instruments share five core components: 1.) a strong electromagnet that produces a homogenous magnetic field (termed B_0); 2.) a radiofrequency (RF) transmitter that produces electromagnetic radiation; 3.) a RF receiver that detects signals from resonating nuclei; 4.) a console that controls the RF pulses and converts the signals into a digital format; and 5.) software to interpret the data produced by the instrument.

NMR uses RF pulses to transfer energy to NMR-active nuclei, causing them to precess and generate a signal. This signal then undergoes a free induction decay (**Fig. 12**), and the rate of this decay determines the rate the instrument can apply the RF pulses. Nuclei in different chemical environments will precess at different rotational frequencies, and these rotational frequencies correspond to different chemical shifts in a full NMR spectra. In MRI, the resonance frequency in the presence of a magnetic field gradient determines the signal location, while the intensity of the MRI signal is dependent on the rate at which the nuclei signals decay and/or grow back.[26–31]

To run a scan, the computer is programmed with the appropriate pulse sequences and experimental parameters then sends this information to the instrument so it may begin the acquisition. The information in the signal that is produced from the sample or patient is extracted

with a demodulator and sent through an analog-digital converter so that the computer can understand the data. The computer then applies a Fourier transform along with other data processing techniques to obtain the final MR image.[32]

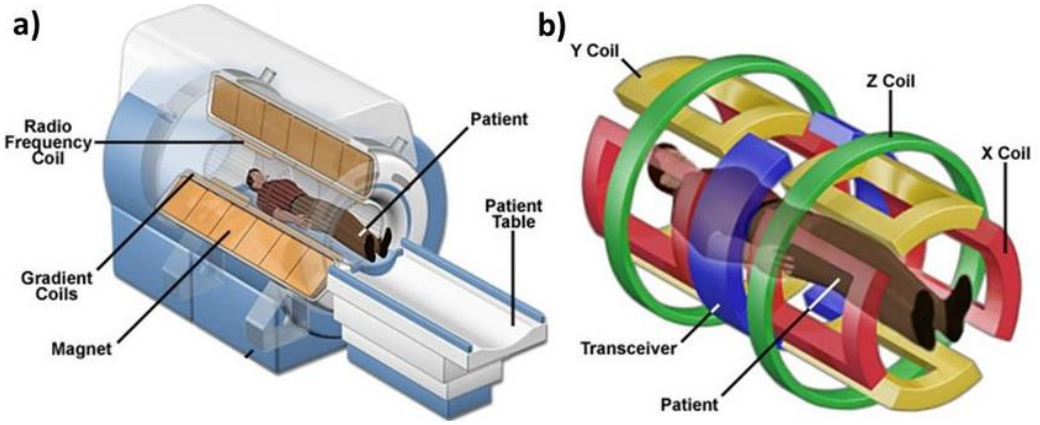

Figure 11: Diagram of a typical MRI instrument (a) and magnetic coils housed inside (b) which generate and detect the magnetic fields during each scan. Image credit: National MagLab.[33,34] Used with permission.

MRI instruments generate a constant, non-fluctuating magnetic field (referred to as B_0) and apply repeating RF pulse sequences using various magnetic coils (**Fig. 11b**) to manipulate nuclei with magnetic spins (such as ^{1}H, ^{2}H, ^{13}C, and ^{14}N). The direction of the homogenous B_0 field is the designated z-axis that the nuclei align themselves with in a parallel fashion. In a typical RF pulse sequence, once the nuclei are aligned within the B_0 field, they are rotated 90° degrees into the xy-plane with a RF pulse. Any protons that have components that are not aligned with the z-axis generate a signal that can be detected by the RF receiver. Immediately after, they begin to precess along the z-axis as they start to realign with B_0. Eventually, the nuclei will return to equilibrium where their signal reaches zero. This is the free induction decay of the signal. (**Fig. 12**)

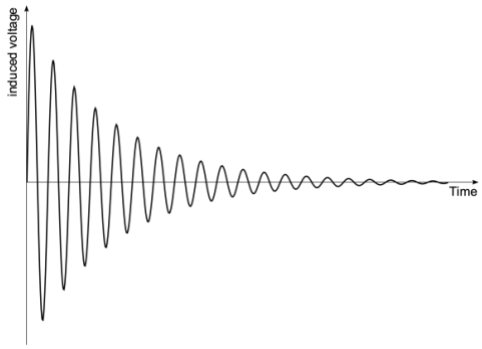

Figure 12: (Above) Typical free induction decay which, after a Fourier transform is applied, gives a signal at a specific frequency. (From Wikipedia and used as-is under a CC BY-SA 3.0 license.)

T_1 and T_2 Relaxation

T_1 and T_2 are characteristics that describe the ways in which ^1H signal decays after being tipped into the xy-plane. Both occur in tandem; There cannot be one without the other. The relaxation time constant T_1 describes how long it takes the longitudinal signal to recover ~63% of its initial value and occurs due to the net magnetization of the ^1H spins realigning with B_0. **(Fig. 13)** The time constant T_2 describes how long it takes the signal to irreversibly decay to 37% of its initial value and occurs due to ^1H spins spreading out in all directions (i.e., dephasing) across the xy-plane **(Fig. 14)**.

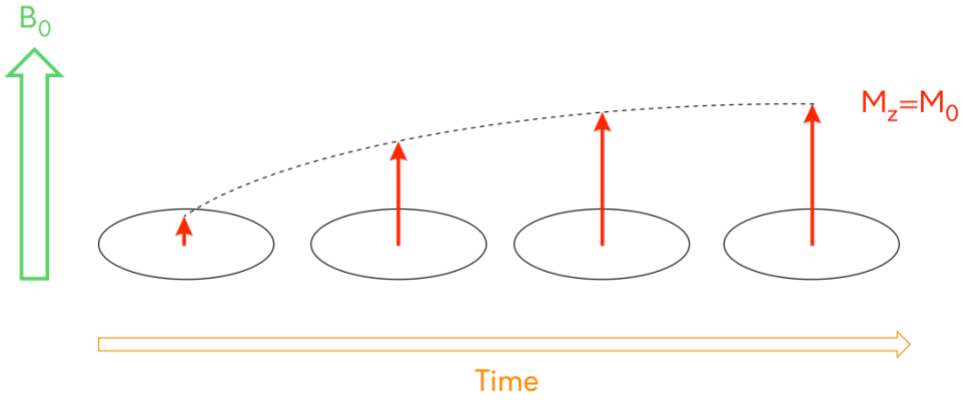

Figure 13: (Above) T_1 relaxation diagram showing net magnetization vector returning to equilibrium with B_0 field following a RF pulse. In T_1 relaxation, signal decay is due to protons realigning with B_0.

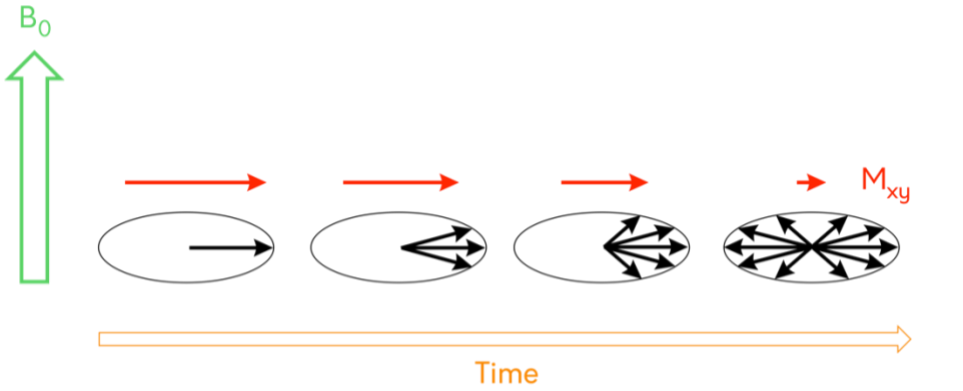

Figure 14: (Above) T_2 relaxation diagram showing dephasing of spins in the xy-plane following a RF pulse. In T_2 relaxation, signal decay is due to proton spins dephasing and spreading out in all directions across the xy-plane.

The clinical CAs currently available today are considered low relaxivity and tend to have r_1 values of ~4 $mM^{-1}s^{-1}$ **(Fig. 15)** whereas high relaxivity CAs are reported to have r_1 values upwards of

and 8-10 $mM^{-1}s^{-1}$. This increase in r_1 value between low and high relaxivity CAs means each individual CA molecule is that much more effective in enhancing MRI contrast.[27]

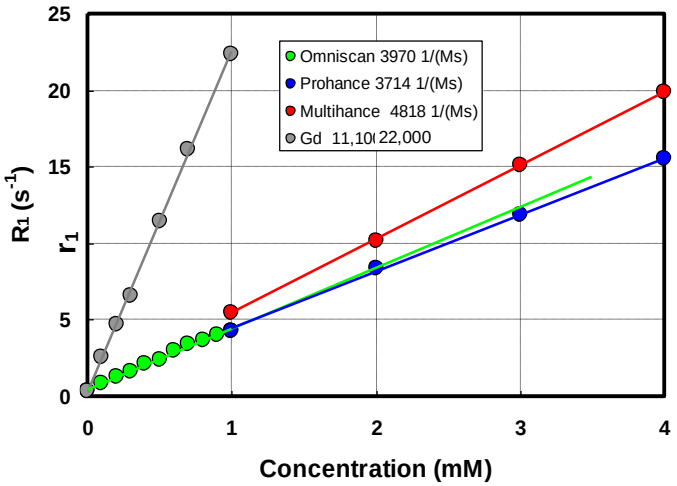

Figure 15: (Above) T_1 relaxivities of some commercial MRI CAs compared to free Gd^{3+} (gray). Data initially published by Dr. Joseph Hornak at RIT.

The relaxation of protons occurs due to energy transfer from the magnetic dipole of a paramagnetic ion (Gd^{3+}, in this case) to the protons themselves.[13] Molecular parameters such as hydration, water exchange kinetics, and correlation time of a particular chelation complex are the three main factors that affect the extent to which this energy is transferred.[13] Water can exist in any of the three coordination spheres of the complex (the inner coordination sphere, the second coordination sphere, and the outer coordination sphere). Hydration number refers to the number of water molecules that can coordinate to the metal ion. The relaxivities of the water protons in all three spheres come together and contribute towards the overall r_1 of the complex. However, only water in the inner-most sphere is able to coordinate directly with the metal.[35,36] (**Fig. 16**) Another parameter than affects r_1 is rotational entropy. Rapid rotational motion and tumbling in solution produce additional magnetic fluctuations which results in a decreased relaxivity rate.[13] These factors influence the time it takes water protons to realign themselves within the B_0 field, and therefore how long a ^1H signal will last in one area of the body versus other areas. Hence the term "contrast", these differences are visualized as dark and light regions in the final MR image and correspond to slower and faster r_1 values, respectively.

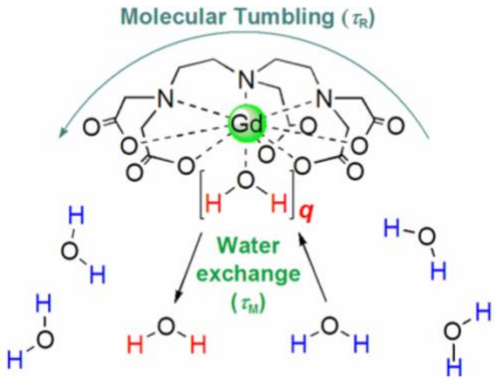

Figure 16: (Above) Diagram of water molecules in the outer and inner coordination spheres of a CA.[37] (Used with permission from Werner et al.)

Contrast Agents and Their Limitations

Contrast agents coordinate to water molecules and cause their protons to respond to magnetic field fluctuations at much faster rates than the protons of water molecules which do not coordinate with them. In other words, they shorten the relaxation time constant (T_1) of water protons, and better CAs shorten T_1 to a greater extent per molecule of agent. Relaxation *time* constants are the inverse of relaxation *rate* constants, so the inverse of T_1 is the relaxation rate constant R1. (**Fig. 17**) However, the T_1 and R1 of a given CA vary with how much of the agent is present and therefore must be related to concentration. This function is the relaxivity, or r_1, of the CA, and it describes how the relaxation rate constant, R1, changes as a function of its concentration. Thus, r_1 is expressed in units of inverse millimolar seconds ($mM^{-1}s^{-1}$).[13,37] (**Fig. 18**)

$$R1 = \frac{1}{T_1}$$

Figure 17: (Above) Equation for relaxation rate constant.

$$r_1 = \frac{\Delta\left(\frac{1}{T_1}\right)}{\Delta[M]}$$

Figure 18: (Above) Equation describing T_1 relaxivity (r_1). CAs cause T_1 to decrease which increases the $1/T_1$ value, thus increasing r_1.

Most of today's clinically used CAs are small molecules (MW of approx. less than ~500-600 g/mol) containing the heavy metal Gd^{3+} held by a chelation complex. Gadolinium is used because its paramagnetic properties are what make it effective at increasing the MR signal. The seven unpaired electrons of Gd^{3+} give it a high magnetic moment, making it an ideal candidate to be used as a CA.[37] Chelators used in MRI contrast agents for Gd can be classified into two main types of structures: Linear and Macrocyclic. As their names suggest, linear chelators by themselves are open chains that wrap themselves around a metal ion whereas macrocyclic chelators already have a set ring structure that is made to fit one metal ion inside them.

1,4,7,10-tetraazacyclododecane-1,4,7,10-tetraacetic acid (DOTA) (**Fig. 19**, left) is a macrocyclic chelator that has been used extensively in our group for chelation of Gd. DOTA has four acetic acid groups that each offer one point of attachment for the Gd metal. These four acetic acid groups, along with the lone pairs on the four nitrogen atoms of the ring, fill all eight of Gd's chelation sites and hold it very tightly within an octadentate coordination. For the dissociation reaction ML → M + L where M is the metal, L is the ligand, and ML is the metal with bound ligand, DOTA was found to have a very high thermodynamic stability of log*K* of ~25.3.[38,39] It is important that Gd does not fall out of its chelation because free-floating Gd^{3+} metal in the body is toxic to the kidneys. Similar to DOTA, 1,4,7,10-tetraazacyclododecane-1,4,7-tris(tert-butyl acetate) (DO3A) (**Fig. 19**, middle) is also a macrocyclic chelator except it does not have a fourth acetic acid arm like DOTA. Even so, the short alanine side chain that our target compound is based upon positions the chelation complex close enough to the amino acid backbone that the coordinated Gd^{3+} can reach the C-terminus and use it as its eighth chelation site.[38] (**Fig. 19**, right)

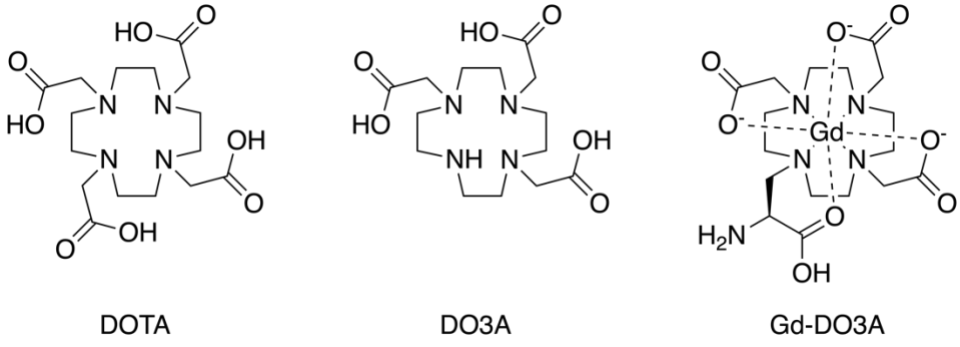

Figure 19: (Above) Structures of macrocyclic chelators DOTA (left), DO3A (middle), and Gd-DO3A (Dotarem). (right)

The r_1 relaxivities of current CAs fall around the range of 4-5 $mM^{-1}s^{-1}$ and are typically administered at a standard dose of 0.1 mM/kg (approximately 0.2 mL/kg) at 10 mL per 15 seconds to enhance contrast.[40] Despite the progress in cancer diagnosis and treatment that these organometallic structures can be attributed to, there are a few main issues with today's CAs that cannot be overlooked. Many of today's CAs lack cell-specific targeting, enabling them to freely travel throughout the entire circulatory system.[27,35] At best, some can only target a single organ system or ubiquitous cellular structure, but this is often still not good enough to achieve earlier cancer detection. This limitation increases the concentration that is required to be present in the body for the MR instrument to produce a usable image. The duration of an MRI lasts anywhere from 15 to 45 minutes (although some can take an hour or more).[35,37,40] For patients that need multiple MRI scans to monitor their malignancy, this can add up to a significant amount of CA that is administered intravenously. Lastly, the high toxicity of unbound Gd^{3+} is due to its ionic radius which is similar to that of calcium, giving it a high affinity for Ca^{2+} ion channels.[37] Since Ca^{2+} is crucial for nerve transmission, muscle contractions, blood coagulation, and the function of mitochondria, free Gd^{3+} can disrupt these biological systems and negatively impact health.

Overall, linear chelators have lower chelating stability than their closed-chain counterparts, making it more likely for Gd^{3+} to dissociate from the complex and freely circulate the body. Linear chelators are associated with nephrogenic system fibrosis, a potentially life-threatening disease that is caused by free Gd^{3+} ions and results in progressive tissue fibrosis across the entire body.[38] Examples of these open chain complexes are Magnevist, Omniscan and OptiMARK, as shown in the top and bottom rows of **Figure 20** below. In one study, in patients with normal renal function, only those who received linear-type Gd CAs were found to have Gd^{3+} deposition in certain brain regions. While there were no observable symptoms in response to Gd^{3+} deposition in the brain in this particular study, it is in the best interest of patient safety that any unintended Gd^{3+} deposition be prevented as much as possible.[39] Furthermore, a 2019 study described the toxic effects that Gd^{3+} CAs can have on mitochondrial function and cell viability in basal ganglia cells.[41] Therefore, the design of new CAs must take into consideration patient safety and minimize the risk of Gd falling out of its chelation as much as possible.[38]

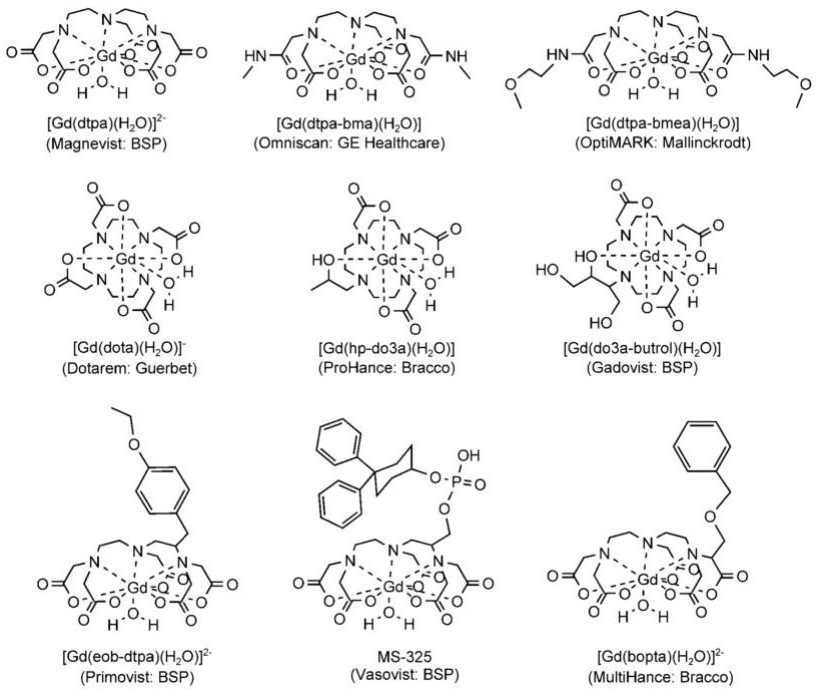

Figure 20: (Above) A selection of commonly used commercial aminocarboxylate-based MRI CAs.[37] Used with permission from Werner et al.

So far, CAs from our work have possessed r_1 values similar to those of commercial agents. However, we previously achieved high relaxivity by attaching two low-relaxivity complexes to the same molecule. The red line on the graph in **Figure 21** below shows our previously synthesized Di-Lys(Gd-DOTA) which we found had an r_1 of 11.33 $mM^{-1}s^{-1}$. While effective, the use of two Gd atoms per CA does not help reduce the amount of metal ion entering a patient's body. Therefore, designing *single* chelate CAs that are more effective at increasing r_1 is a superior approach.

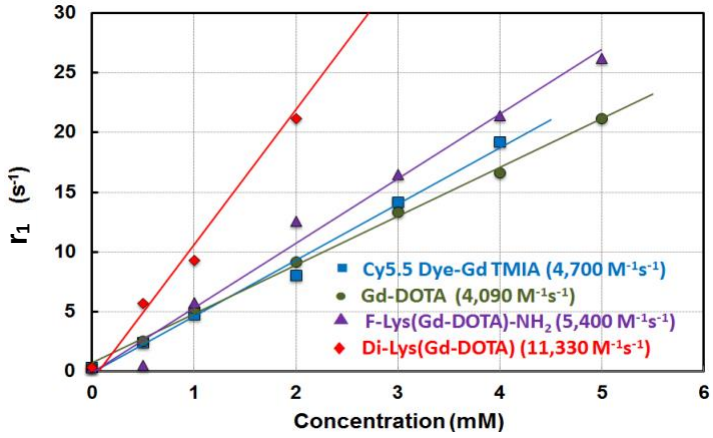

Figure 21: (Above) T_1 relaxivities (r_1) of CAs from our previous work compared to Dotarem (green).

Synthetic Approach

Modular Approach to TMIA Synthesis

Our group synthesizes modular compounds for molecular imaging. The synthetic design splits these modules into two groups based on their functionality: imaging modules and targeting modules.[42] Due to the modular nature of these structures, all of them can be linked to one another through simple coupling reactions to construct a targeted molecular imaging agent (TMIA) for a particular imaging modality to target a specific biomarker. (**Scheme. 1**) For these applications, amino acids are favorable due to their bioavailability and biostability.[43] Additionally, since the reagents, methods, and coupling mechanisms for peptides are well known, we can focus on developing new TCAs instead of new reactions. In our earlier work, the lysine side chain was chosen to attach the DOTA chelating group for imaging.[42] However, for our current purposes, alanine is chosen instead because its shorter chain length allows Gd to chelate to the amino acid backbone, lowering the rotational entropy of the complex and contributing towards higher T_1 relaxivity.[13,27,35–37] This new chelation complex design would require the development of a new synthetic route to modules (i.e. "puzzle pieces") containing the rotationally restricted alanine analogs.

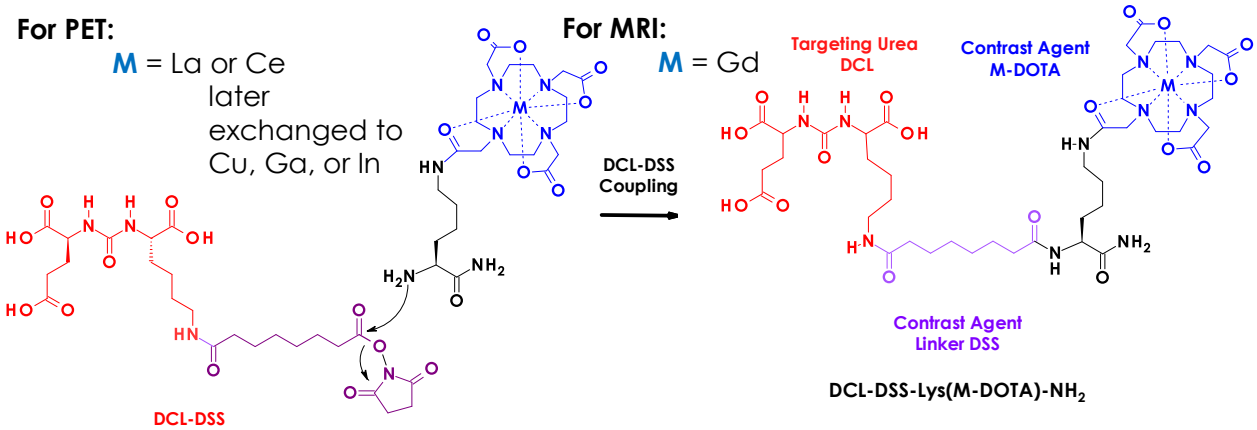

Scheme 1: General synthetic approach for TMIAs using DCL pre-coupled to DSS linker. The metal (shown as M) can easily be customized depending on the desired imaging modality.

Synthetic Approach to High Relaxivity Contrast Agents

Previously, contrast agents in our group have been built using a lysine derivative that is N-terminally protected by Fmoc because it is inexpensive and can be incorporated easily into solid phase peptide synthesis (SPPS). Additionally, its primary amine side chain is easily coupled to chelating groups (such as DOTA) which hold metal ions, allowing the molecule to be used with various imaging methods depending on the metal that is chosen.[42,44–46] While lysine works as a starting place upon which to construct a CA, it is not a suitable scaffold from which to build one of high-relaxivity because of the long 4-carbon chain (**Fig. 23**, pink) between the chelation complex and amino acid backbone. This distance makes it difficult to control the rotational entropy, one of the molecular parameters that affects a contrast agent's ability to increase r_1.[35,36]

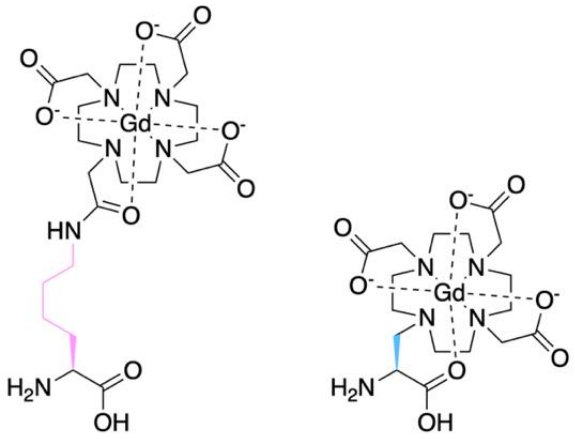

Figure 23: (Above) Structures of CA modules based on Lysine (left) and Alanine (right).

Novel Use of Metals as DO3A Protecting Groups

In this approach, the three free acid groups of DO3A can be protected from unwanted reactivity by chelating Gd^{3+} early in the synthesis. This early chelation allows the metal to prevent the carboxylic acid arms from participating in unwanted side-reactions. Other synthetic approaches leave these arms protected by tert-butyl groups and cleave them in the final steps with TFA just before the metal chelation step. The downside of this approach is that this exposes the entire TMIA to the harsh conditions of TFA, thus risking its decomposition. The removal of t-butyl groups on DOTA was found to require exceedingly harsh acid (100% TFA) compared to isolated esters (such as on the side chain of glutamic acid) which only requires just 10% TFA. Such harsh treatment has resulted in degradation of precious peptides in our lab. The early metal chelation

avoids harsh deprotection conditions on the final TMIA and reduces the risk of degrading the overall TMIA. This method of chelating the metal early has been utilized by our group extensively with DOTA and is shown to be just as reliable with DO3A.

Evaluation and Analysis of Compounds

Compounds were assayed and characterized with liquid chromatography-mass spectrometry (LC-MS), and high-resolution mass spectroscopy (HRMS). T_1 relaxivity experiments of compounds were run on a 43 MHz Magritek NMR spectrometer. Details of these methods can be found in the experimental section.

Results and Discussion

Schemes 2a and **2b** outline the synthetic design we envisioned and embarked upon. **Scheme 2a** is a modification of the approach by Boros et al.[35] which seeks to introduce the Gd early in the synthesis (step vi) and remove the t-butyl groups early (step iv) rather than after the module is coupled to a peptide. Our modular approach only utilizes the t-butyl groups in the assembly of the precursor to the Ala(DO3A) macrocyclic chelator. By immediately removing these groups and chelating Gd early in the synthesis (step viii), we eliminate any chance of exposing the final HR-TCA to the brutal t-butyl deprotection conditions known to be destructive to peptides.

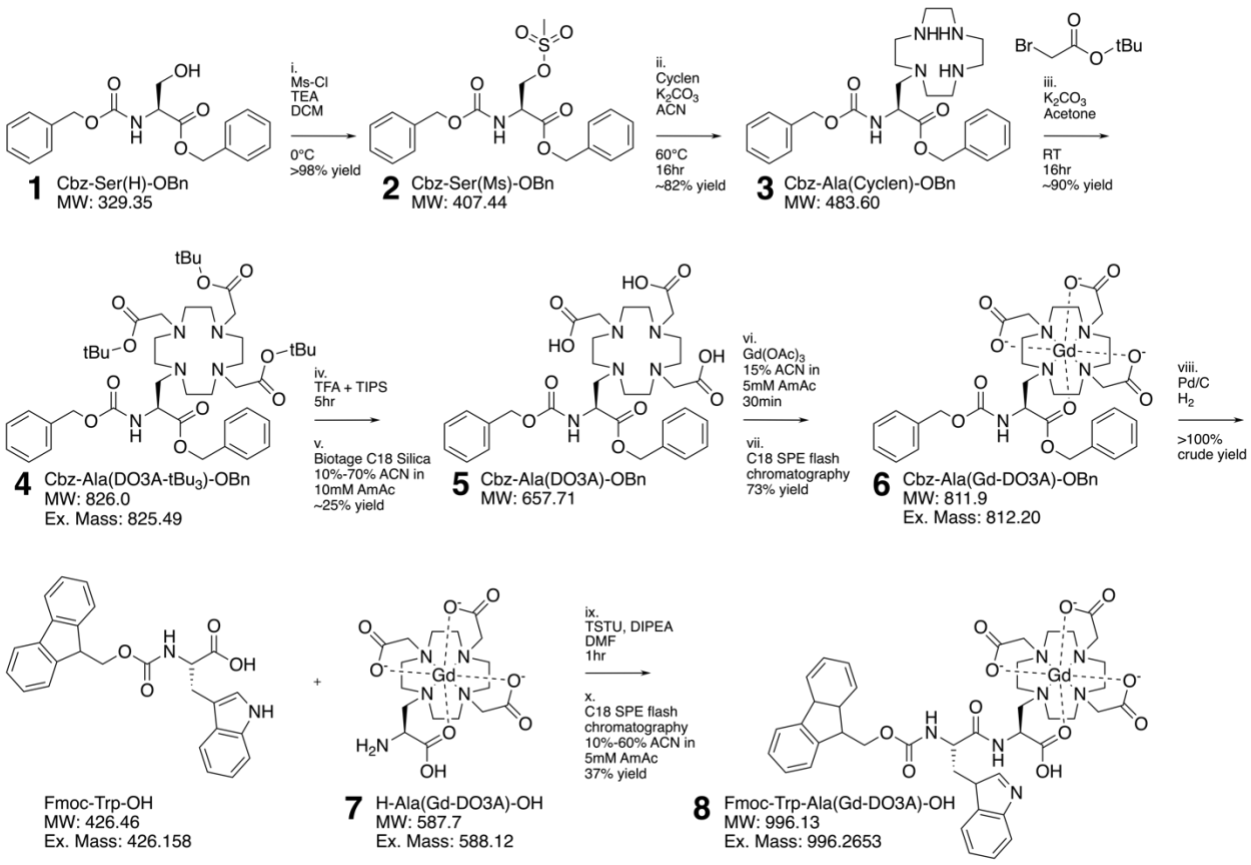

Scheme 2a: (Above) Part 1 of the reaction schematic for the proposed HR-TCA.

The synthesis began with Cbz-Ser(H)-OBn (1), a commercially available Serine derivative that is protected at the N-terminus by a carboxy benzyl group and protected at the C-terminus by a benzyl group. The side chain was then reacted with methane sulfonyl chloride (1.2 eq) in DCM under basic conditions (1.6 eq TEA) to afford the crude Cbz-Ser(Ms)-OBn (2) which was easily purified by liquid-liquid extraction and obtained at >98% yield. (Scheme 2a, step i)

Mesylate groups are excellent leaving groups and easily displaced by primary and secondary amines such as those in cyclen, an aza-crown ether. Displacement of the mesylate group by cyclen formed the foundation for the macrocyclic chelation complex, Cbz-Ala(Cyclen)-OBn (3). (Scheme 2a, step ii) This was run by dissolving excess cyclen (4 eq) into ACN with1.5 eq of inorganic base K_2CO_3 and heating the mixture to 65°C. Once heated, compound 2 was dissolved in ACN, added dropwise, and allowed to react for 16 hours. When completed, compound 3 was purified with liquid-liquid extraction and obtained in approximately 82% yield.

The remaining three secondary amine groups of the cyclen ring were alkylated by dissolving Cbz-Ala(Cyclen)-OBn (3) in acetone with K_2CO_3 (1.5 eq) and tert-butyl bromoacetate

(3.2 eq). (**Scheme 2a**, step iii) The mixture was allowed to react for 16 hours at room temperature and then was purified with liquid-liquid extraction to afford Cbz-Ala(DO3A-tBu_3)-OBn (**4**) at 90% yield.

Tert-butyl groups were removed by dissolving **4** into pure TFA and adding 2 eq of TIPS as a hydride donor to counteract formation of the tert-butyl radical cation. (**Scheme 2a**, step iv) The reaction was allowed to react for a maximum of 5 hours. Its progression was monitored by taking hourly aliquots of the mixture, removing the TFA *in vacuo*, and assaying in LC-MS. The reaction was deemed finished when the product peak 658.14 m/z appeared as the base peak while mass peaks 714 m/z and 770 m/z of intermediates Cbz-Ala(DO3A-tBu_1)-OBn (**4b**) and Cbz-Ala(DO3A-tBu_2)-OBn (**4c**) (**Fig. 24**), respectively, were no more than 15-20% of the total ion intensity. To stop the reaction, the entire reaction flask was attached to a rotary evaporator to remove the bulk of the TFA. When the initial reaction volume was reduced as much as possible, ~10-20 mL of ACN was added and the mixture was concentrated *in vacuo* again to continue pulling off any remaining TFA. This rotary evaporation was performed 3-4 times to pull off as much TFA as possible prior to purification on a Biotage Selekt with flash HPLC and Biotage Sfär C18 30g column. (**Scheme 2a**, step v) All fractions were assayed via direct injection mass spectrometry. Pure fractions were collected and concentrated *in vacuo* before being freeze dried to obtain incredibly pure Cbz-Ala(DO3A)-OBn (**5**) in 24.74% yield.

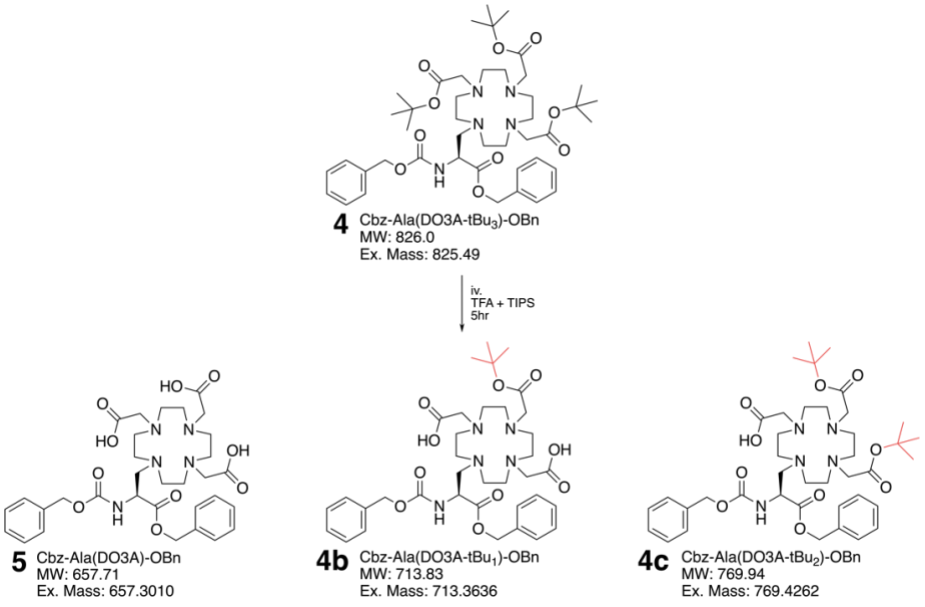

Figure 24: (Above) Diagram of tert-butyl deprotection showing the formation of desired product (**5**), and mono- and di-tert-butyl intermediates **4b** and **4c**, respectively.

To chelate Gd, freeze dried compound **5** was combined with 3 eq of $Gd(OAc)_3$ in 5mL of 15% ACN in 5mM AmAc buffer (**Scheme 2a**, step vii). The mixture was then purified via flash chromatography on C18 silica using a gradient of 10%-50% ACN in 5mM AmAc buffer increasing in concentrations of 10%. Pure fractions were concentrated *in vacuo* and freeze dried to afford compound **6** in 73.4% yield. Compound **6** represents the departure from the literature approach by Boros et al (ref) as the Gd module replaces the t-butyl protected chelator, DO3A, in the remainder of the synthesis. As described earlier, the protection of the DO3A by the Gd metal itself avoids the harsh deprotection steps required at a later time point in the synthesis where the valuable peptide has been assembled.

Removal of the carboxybenzyl and benzyl protecting groups of Cbz-Ala(Gd-DO3A)-OBn (**6**) was first attempted via catalytic hydrogenation with formic acid, 20% Pd/C, and H_2 gas, but the success rate of this method proved too slow to be practical and often left the carboxybenzyl group untouched. We resorted to removing the carboxybenzyl and benzyl protecting groups with palladium black and vigorous H_2 gas in methanol. Compound **6** was combined with 1 eq Pd Black in MeOH and allowed to react for 1 hour while H_2 gas was rigorously bubbled into the reaction. Upon completion, the reaction mixture was filtered then concentrated *in vacuo*. Not all catalyst was able to be removed from the crude reaction and most likely contributed to excess yield. The remaining residue was freeze dried to afford H-Ala(Gd-DO3A)-OH (**7**) in > 100% yield. (**Scheme 2a**, step viii)

Use of Tryptophan as a Spacer

After initial synthetic attempts to couple the H-Ala(Gd-DO3A)-OH (**7**) directly to the linker and targeting group, we decided to couple an Fmoc-protected tryptophan to H-Ala(Gd-DO3A)-OH (**7**) to add hydrophobicity in an attempt to assist with separation of the final HR-TCA (**10**) on C18 silica. The addition of the tryptophan also increases lipophilicity, enhancing bioavailability and cell permeability. Additionally, tryptophan's absorption of 270nm wavelength light would assist in visualizing the product on HPLC. Furthermore, we suspect that the increase in molecular weight would decrease the overall molecular tumbling rate in solution and provide another means by which the relaxivity is enhanced.

To synthesize compound **8**, 1 eq of Fmoc-Trp-OH was first combined with 20 eq of DIPEA, 1.2 eq of coupling agent TSTU, and ~10 mL of DMF in a reaction flask in order to activate the carboxylic acid for coupling. Prior to addition of compound **7** to this mixture, Fmoc-Trp-OH was first confirmed to be properly activated. This was done by removing a 20-minute aliquot of the mixture, crashing it out of solution with diethyl ether, spinning down the precipitate, and removing the decant. To the precipitate, one drop of 0.1% aqueous octylamine was added and one drop of this was placed into an HPLC vial and filled the rest of the way with diH_2O. The prepped aliquot was assayed with both direct injection mass spectrometry and LC-MS. When only Fmoc-Trp-Octylamine molecular weight in positive ion (538 m/z) mass spec is observed with no Fmoc-Trp-OH starting material, the activation mixture was deemed ready to be combined with H-Ala(Gd-DO3A)-OH (**7**). To a separate flask or vial, compound **7** was first dissolved into 5-10 mL of DMF with 20 eq of DIPEA and then added to the activated Fmoc-Trp-OH mixture and allowed to stir for about 1 hour. When finished, the reaction mixture was concentrated *in vacuo* to remove ~50% of the DMF. The product was crashed out of solution with diethyl ether, vortexed, and centrifuged. The supernatant was discarded and the precipitate, crude Fmoc-Trp-Ala(Gd-DO3A)-OH (**8**), was dried under $Ar_{(g)}$ and then run through reverse phase C18 SPE with 10%-60% ACN in 5mM AmAc increasing in 5% increments. (**Scheme 2a**, step ix) The pure fractions were combined, concentrated *in vacuo*, and freeze dried to obtain pure Fmoc-Trp-Ala(Gd-DO3A)-OH (**8**) in 36.96% yield. (**Scheme 2a**, step x)

Compound **8** was dissolved into DMF with 24 eq of diethylamine (DEA) base. Immediately after combining, the pH was confirmed to be sufficiently basic (pH of at least 10). The reaction was run for 2 hours, at which time the compound was crashed out of solution with diethyl ether, vortexed, and spun down. The supernatant was discarded, and the precipitate was dried under $Ar_{(g)}$. The precipitate was dissolved into diH_2O with 1 µL of TEA and then freeze dried overnight to afford H-Trp-Ala(Gd-DO3A)-OH (**9**) at 75-77.78% yield. (**Scheme 2b**, step xi)

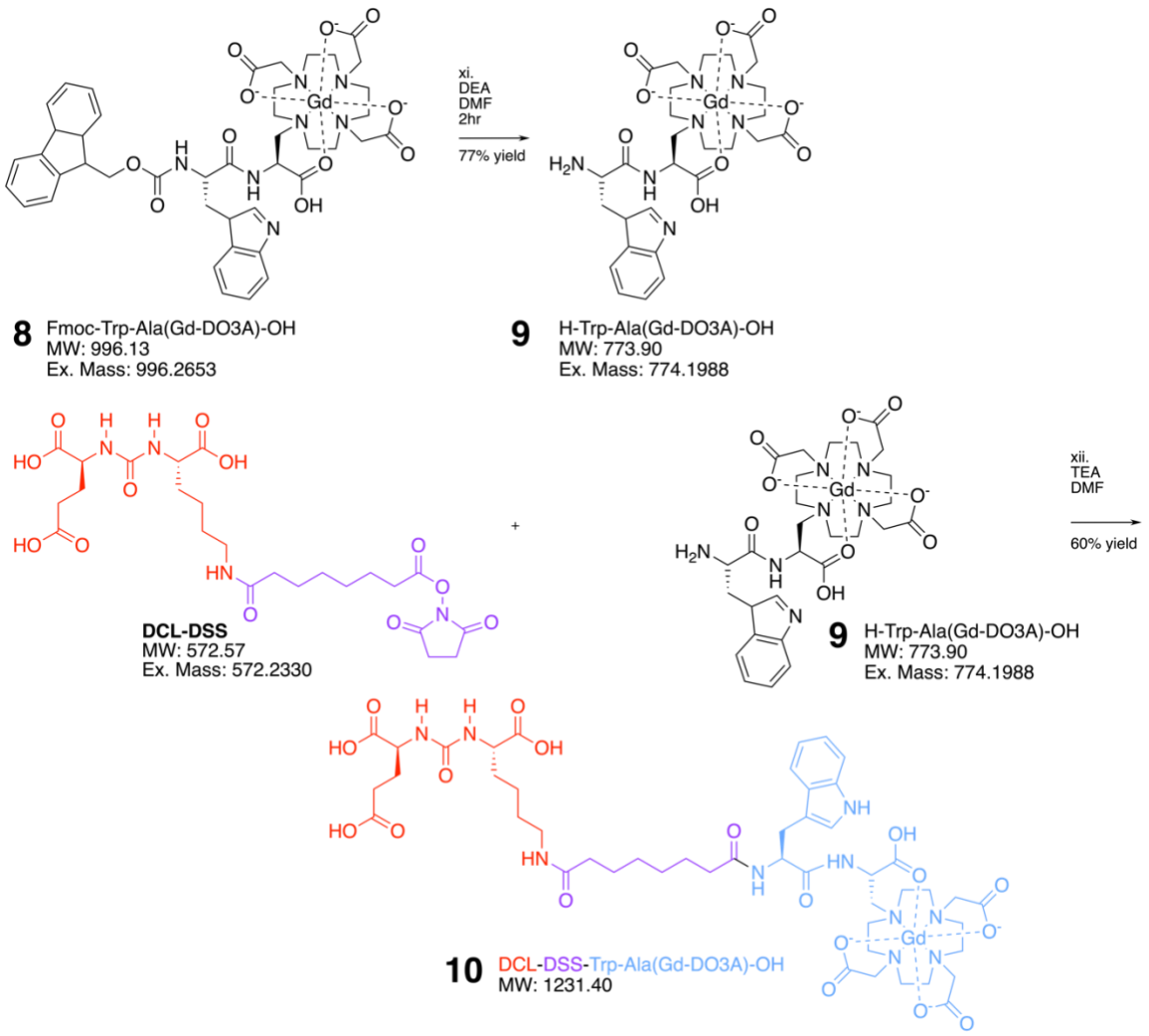

Scheme 2b: (Above) Part 2 of the reaction schematic for the proposed HR-TCA.

Step xii in **Scheme 2b** above outlines the convergent point of our synthetic approach: The convergent coupling of the premade DCL targeting group (red) with the DSS linker (purple) to compound **9**. This was done by dissolving compound **9** into DMF with 10 eq of TEA under $Ar_{(g)}$. Once dissolved, 1 eq of the premade DCL-DSS was added and allowed to react for 2-3 hours. When finished, the product (now crude compound **10**) was crashed out of solution with diethyl ether, vortexed, and centrifuged before drying over high vacuum overnight. The dried crude compound **10** was run through a manual C18 flash chromatography with 2-30% MeOH in 5mM AmAc, increasing in 2% increments. Pure fractions were combined, concentrated *in vacuo*, and freeze dried. The compound was redissolved again in a small volume of diH_2O and filtered through a 0.3 µm syringe filter and then freeze dried a second time. Once more, the compound

was redissolved in diH_2O, filtered through a fresh 0.3 μm syringe filter, and then freeze dried for the third and final time to obtain the final HR-TCA, DCL-DSS-Trp-Ala(Gd-DO3A)-OH (**10**), at 60.4% yield.

The Struggle of Optimizing the tert-Butyl Deprotection with TFA

The true struggle of this synthesis was the removal of the tert-butyl protecting groups. The literature method outlines using a mixture of DCM and TFA heated to 55°C. (**Table 1**, Trials 1-2c) This method was found to generate nothing but impurities with no semblance of product. In fact, we discovered that addition of DCM to the reaction slowed progress so much that it became impractical to even consider using a TFA concentration of anything less than 90%.

Removal of the tert-butyl group results in generation of unstable tertiary carbocations. Radical scavengers were investigated as a means of avoiding accumulation of the tert-butyl radical. Various trials of pure TFA solvent with varying amounts of anisole were run, but this was also unsuccessful and showed no improvement. (**Table 1**, Trials 2a-2c) Over the course of just 30-60 minutes, the mixture also showed evidence of oxidation due to its appearance changing to a dark brown similar to that of black earl grey tea. Thus, it was concluded that a more generous flow of argon gas should be used to prevent oxygen reactivity at the surface of the solution as much as possible. Next, we tried plain TFA by itself at room temperature and ensured a vigorous flow of $Ar_{(g)}$ gas was maintained over the reaction for its entire duration. This resulted in greater than 100% yield and many impurities. No product peak or any other recognizable peaks could be identified when analyzed by LC-MS. In a desperate attempt to see any semblance of product formation, the reaction was placed into the freezer overnight which unsurprisingly was not helpful. However, the lack of any significant oxidation (i.e., the reaction solution remained exceptionally clear and transparent, similar to that of raw egg whites) could have been attributed to the higher argon gas flow. (**Table 1**, Trial 3)

Yet another series of tert-butyl deprotection trials were performed to see if Gd could be chelated alongside the deprotection step using various ratios of DCM, $Gd(OAc)_3$, and TFA. (**Table 1**, Trials 4a-4c) While one of the trials was shown to contain the chelated compound **6**, yield was abysmal, and LC-MS showed a base peak of an impurity with 716 m/z in positive ion mode.

(**Scheme 3**) Therefore, it was concluded that it is not possible to chelate Gd into the crude reaction.

Diving into literature revealed mixtures of TFA, dithiothreitol (DTT), TIPS, and H_2O to create a "Cleavage Cocktail" that is typically used in solid phase peptide synthesis and is formulated specifically for a particular peptide and its protecting groups. They are used to simultaneously remove protecting groups and cleave the peptide from its resin. The first attempt of using this Cleavage Cocktail was unsuccessful, but the second attempt (**Table 1**, Trial 5) showed promise in formation of mono- and di-tert-butyl intermediates (previously shown in **Figure 24**). After many reformulations of the Cleavage Cocktail (Trials 5-12, Trials 10-11 not shown), progress finally showed with a taller product peak and decreased peaks of side reaction byproducts and impurities. (**Table 1**, Trials 6-9) Attempts were made to use other protecting groups such as ethyl and benzyl by instead reacting the free amines of Cbz-Ala(Cyclen)-OBn (**3**) with ethyl and benzyl bromoacetate, respectfully. All attempts to remove these protecting groups were unsuccessful. Therefore, the decision was made to stick with the tert-butyl protecting group approach.

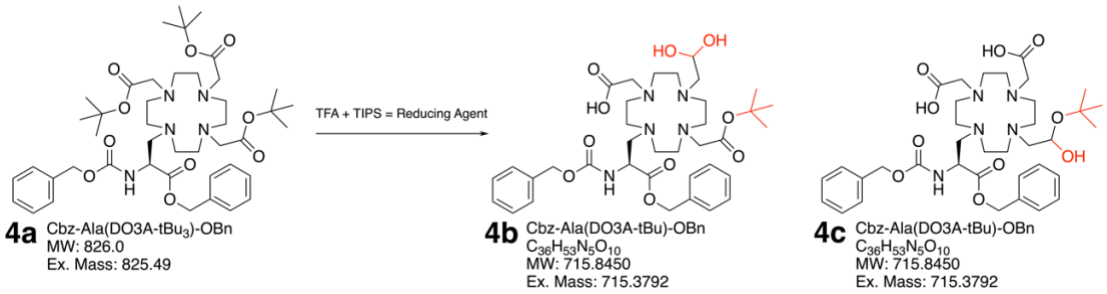

Scheme 3: (Above) Potential unwanted side reaction caused by TFA and TIPS possibly forming a reducing agent and transforming one of the t-butyl esters into either an acetal (**4b**) or hemiacetal (**4c**) in extreme acidic conditions.[47]

Many more tert-butyl deprotection trials resulted in the reaction time being limited to 5 hours since anything more was found to result in a messy spectra and significantly lower yields. Eventually, it was discovered that use of DTT in the Cleavage Cocktail could potentially have negative downstream effects on the synthesis. Any residual DTT remaining with compound **5** following tert-butyl deprotection could possibly poison the metal catalyst during the Pd catalyzed hydrogenation of step viii in **Scheme 2b**. This was hypothesized because it was near impossible to remove the Cbz and Bn protecting groups from one specific batch of compound **6** whose lineage could be traced back to a batch of Cbz-Ala(DO3A)-OBn (**5**) that was obtained by using the DTT-containing Cleavage Cocktail. In comparison, all batches of Cbz-Ala(DO3A)-OBn (**6**) whose

precursor compound *5* was obtained using deprotection conditions of *only* TIPS+TFA always progressed. It was decided at this point to forego use of the Cleavage Cocktail in favor of only 2 eq of TIPS to counteract formation of the radical cation and prevent any downstream consequences of the sulfur-containing compound potentially hindering the Pd catalyzed hydrogenation. (**Table 1**, Trial 15)

Ultimately, the tert-butyl deprotection required the use of pure TFA as the solvent, along with 2 eq of TIPS as a hydride donor and radical scavenger. While this deprotection step was the most grueling and time-consuming step of the synthesis to work out, the optimized procedures were able to afford Cbz-Ala(DO3A)-OBn (*5*) in yields ranging from 12.9%-24.74% at near 100% purity (**Table 1**, Trials 16-20), a huge improvement over the previous < 5% yield at abysmal purity. To overcome the low yield amount, we employed a "go big so we don't have to go back" approach which involved running the tert-butyl deprotection at scales upwards of 3.0-4.0 g to ensure adequate yields of 150-300 mg could be obtained to move forward in the synthesis. (**Table 1**, Trials 18-20) Overall, it took more than 20 runs of the tert-butyl deprotection, at least 18 manual C18 SPE purifications, and months of grueling HPLC method development to achieve these improvements in yield and purity.

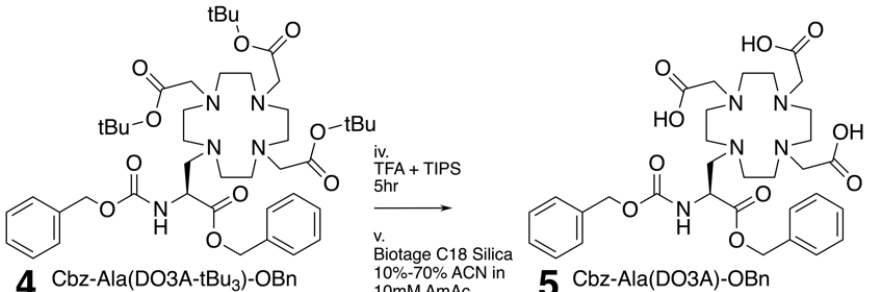

4 Cbz-Ala(DO3A-tBu$_3$)-OBn
MW: 826.0
Ex. Mass: 825.49

5 Cbz-Ala(DO3A)-OBn
MW: 657.71

Trial	Identifier	Scale	Crude % Yield *5*	Pure % Yield *5*	Purity	Important Takeaways for Future Investigators
1	Attempt 1: From Literature	532 mg	14%	N/A	Abysmal	Must use Ar gas. Something must be done about accumulation of tBu carbocation. DCM may slow rxn rate
2	Anisole Trials					Barely any product formation. Anisole is bad. Need faster Ar flow. Abysmal purity.
2a	Flask 1	54.6 mg	N/A	N/A	N/A	
2b	Flask 2	52.0 mg	N/A	N/A	N/A	
2c	Flask 3	51.4 mg	91%	N/A	Abysmal	
3	Ice Bath/Freezer	217 mg	> 100%	N/A	Depressing	Semblance of product formation. Better Ar flow = less oxidation as rxn progresses.

4	Simultaneous Gd Chelation Trials					Never chelate and deprotecting tBu at the same time. DCM slows rxn down too much. Do not use DCM.
4a	Flask 1	50 mg	N/A	N/A		
4b	Flask 2	50 mg	N/A	N/A		
4c	Flask 3	50 mg	N/A	N/A		
5	2nd Cleavage Cocktail	50 mg	N/A	N/A	N/A	Should give Cleavage Cocktail one more chance since we determined the reaction was removed too soon. Already saw good progress in the form of mono- and di- tBu intermediates.
6	"Noche" 2nd Cleavage Cocktail and Excessive TIPS Out of Desperation	167 mg	12.50%	N/A	~20%	Cleavage Cocktail/radical scavengers proving promising. Ran overnight in freezer to try and slow reactivity of tBu radical cation.
7	"Dos Noches" 3rd Cleavage Cocktail	300 mg	16.50%	N/A	~20%	Mass spectra are looking better. Focus is now directed at improving C18 SPE. Cold temp of freezer is hypothesized to help prevent unwanted reactivity.
8	4th Cleavage Cocktail	300 mg	N/A	N/A	N/A	Potentially need to add more Cleavage Cocktail reagents (DDT and TIPS) to better counter radical formation.
9	1st Modified Cleavage Cocktail (Double Mol% of TIPS)	300 mg	> 100%	N/A	N/A	Speculations about why > 100% yield. Unsure if extra TIPS did anything helpful.
12	4th Modified Cleavage Cocktail w/ DCM Trials					The small amt of DCM used to try to slow rxn and decrease bi-product formation did nothing.
12a	Flask 1: 50 mg sm + 5 mL Cleavage Cocktail	50 mg	N/A	N/A	N/A	Impurities everywhere. Maybe we just need better purification.
12b	Flask 2: 50 mg sm + 5 mL 75% Cleavage Cocktail in DCM	50 mg	N/A	N/A	N/A	Never again DCM. Rxn too slow.
13	Cleavage Cocktail: HPLC/SPE Method Development - 500 mg Scale					
13a	"Hail Mary" Biotage	23.7 mg of crude	0%	N/A	N/A	New approach: Optimize purification and go big so we don't have to go back.
13b	HPLC Method Development 1					50:50 mixed solvent system of MeOH:ACN 10%-70% in diH_2O did not improve peak separation. MeOH 30-70% seems to work best separating 812 from 716 m/z pos ion.
13c	SPE Method Development 1: Based on HPLC Method Development 1	30 mg of crude	0%	N/A	N/A	Used gradient HPLC Method Development 1. No product recovered. Should try different solvent system.
13d	HPLC Method Development 2					50:50 mixed solvent system of MeOH and ACN 30-70% in diH_2O showed improved peak separation.
13e	SPE Method Development 2: Based on HPLC Method Development 2	40 mg of crude	0%	N/A	N/A	30%-70% MeOH in diH_2O, increasing by 5%. Chelated 1.5 eq Gd. Need to figure out why Gd falls out of chelation. Possible suspects: MeOH, unbuffered solvents, the C18 silica itself. Decide to try buffered SPE solutions.
13f	SPE Method Development 3: Based on Failures from Method Development 2	11.1 mg of crude	0%	N/A	N/A	SPE with 10%-40% ACN in 5mM AmAc. For each conc, collected 3 fracs in 50x100mm test tubes, approx. 12.5mL

	$Gd(OAc)_3$ vs $GdCl_3$					per tube. Fracs sat out in 5mM buffer. Bn first observed to be lost. Gd stayed in. Too much compound lost during SPE to be recovered.
13g	SPE Method Development 4: New bottle of $Gd(OAc)_3$. Test to see whether terminal Bn group is lost in unbuffered solution.	10 mg of crude	0%	N/A	N/A	Chelated 2 eq of new Gd. SPE run 10%-40% ACN in diH_2O, increasing by 10%. 3 50x100mm test tubes per conc, approx. 12.5mL per test tube. Bn is not cleaved in absence of buffer. Too small amt product to be recovered.
13h	Another Biotage	115 mg of crude	12%	N/A	N/A	C18 likely not responsible for loss of Gd. Finally discovered 716m/z is not mono tBu, but *instead* acetal or hemiacetal, aka PUBLIC ENEMY #1. We need use buffer. Identified EVIL MASSES (in pos ion): 716 = 1 tBu, 1 Acetal 772 = 2 tBu, 1 Acetal 774 = 2 tBu, 2 Acetal
14	One Final Cleavage Cocktail	547 mg	17.00%	N/A	Suspicious	Only somewhat improved yield
14a	SPE of Chelated 14	93 mg of crude	11.12%	N/A	N/A	Maybe too much product loss. Perhaps due to silica?
15	No more Cleavage Cocktail					No more DDT.
15a	Biotage of entire Crude Cbz-Ala(DO3A)-OBn	282 mg	N/A	N/A		Possible correlation between amt of TIPS and amt of Public Enemy #1 (716 m/z pos ion) generated during rxn. Less TIPS might = Less 716. Maybe Biotage isn't to be trusted
16	Less TIPS (2 eq)					
16a	Biotage of Unchelated 15	244 mg	N/A	13.45%	> 90%	Progress! Very low yield but improvements in purity make up for it!
17	Go Big So We Don't Have To Go Back					
17a	Biotage of Unchelated 16	584 mg	N/A	10.58%	~90%	Biotage is, in fact, trustworthy
18	Go REALLY Big So We Don't Have To Go Back					
18a	Biotage of Unchelated 17	3200 mg	N/A	12.39%	> 95%	Most optimized procedures to date
19	Go REALLY Big (Again) So We Don't Have To Go Back					
19a	Biotage of Unchelated 18	3700 mg	N/A	7.56%	> 95%	
20	Go REALLY Big (Yet Again) So We Don't Have To Go Back					
20a	Biotage of Unchelated 19	2387 mg	N/A	14.50%	> 90%	

Table 1: (Above) List of selected tert-Butyl deprotection experiments in chronological order, summarized.

To use buffered solution, or not to use buffered solution? That is The Question!

Chelating crude Cbz-Ala(DO3A)-OBn (*5*) with $Gd(OAc)_3$ was shown to never be successful, so a purification with a reverse phase C18 silica is required beforehand. Following collection and rotary evaporation of pure fractions, the purified Cbz-Ala(DO3A)-OBn (*5*) was redissolved in ACN with AmAc buffer and chelated with $Gd(OAc)_3$. The resulting crude Cbz-Ala(Gd-DO3A)-OBn (*6*) was put through a quick reverse phase SPE to get rid of excess Gd. Once Gd is chelated, the compound should never be allowed to sit in unbuffered solution, nor should it ever touch acidic buffer, otherwise Gd falls out of chelation, reverting it back into Cbz-Ala(DO3A)-OBn (*5*). This unintended demetallation is undesired because it requires re-chelation of Gd and yet another SPE on C18 silica, resulting in unnecessary loss of product and time. Alternatively, when Cbz-Ala(Gd-DO3A)-OBn (*6*) is allowed to sit in AmAc buffer for any longer than 2 hours at room temperature, it results in loss of the benzyl group. We suspect this is due to the Gd facilitating hydrolytic cleavage through its coordination bond to the ester of the benzyl protecting group (Scheme 4).

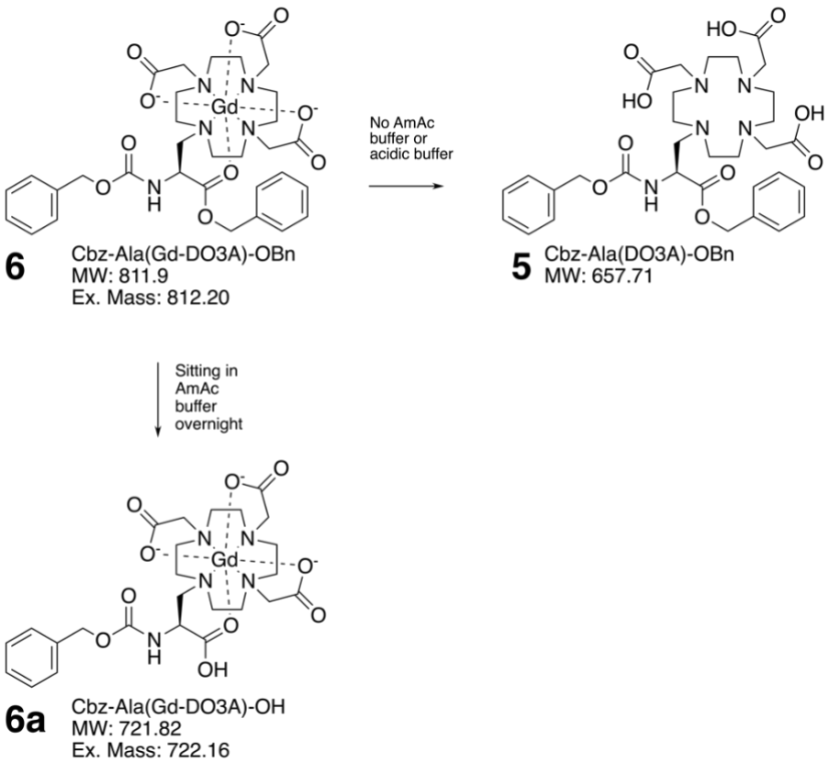

Scheme 4: (Above) Schematic of basic buffer-dependent side transformation of compound 6.

The End Game: Convergent Coupling of Imaging Module to Targeting Module

The coupling of Fmoc-Trp-OH with H-Ala(Gd-DO3A)-OH (**7**) was easily carried out with peptide coupling agent TSTU and purified on C18 silica to afford Fmoc-Trp-Ala(Gd-DO3A)-OH (**8**). A simple Fmoc deprotection with DEA yielded the HR CA module, H-Trp-Ala(Gd-DO3A)-OH (**7**), which was then conveniently coupled to in-house synthesized targeting group and linker, DCL-DSS, to successfully obtain the final HR-TCA, DCL-DSS-Trp-Ala(Gd-DO3A)-OH (**10**). This step completed the designed convergent coupling of the imaging module, H-Trp-Ala(Gd-DO3A)-OH (**9**), to the targeting module, DCL-DSS.

Relaxivity Measurements

The T_1 efficiency of an MRI contrast agent is its spin-lattice relaxivity r_1 in $mM^{-1}s^{-1}$. T_1 relaxivity (r_1) of CA solutions between 0 mM and 5 mM was measured with an inversion recovery pulse sequence, plotted vs. concentration, and relaxivities were measured as the slope.

The details of each set of measurements are in the experimental section below. As observed in the graph in **Figure 25** below, all the agents exhibited a T_1 relaxivity modestly higher than Gd-DOTA (Dotarem) (red) which has a relaxivity of 4.1 $mM^{-1}s^{-1}$. While the modest increase in relaxivity is disappointing, it is speculated that higher relaxivity in the constrained Ala(DO3A) system (as described in the Boros paper[35]) is only realized after a certain critical mass in a longer peptide or by other effects of larger substituents on close-by neighboring side chains.

This speculation is further substantiated by the surprising results exhibited by the Fmoc-dTrp-Ala(Gd-DO3A)-OH (**8**) with substantially higher relaxivity than the other compounds (**Fig. 25**) at the higher concentrations (of 2, 3, 4 and 5 mM). However, the curve itself is not completely linear and appears to be bi-phasic, with similar relaxivity values as the rest of the compounds in the series at lower concentrations (0.5, 1 and 2 mM).

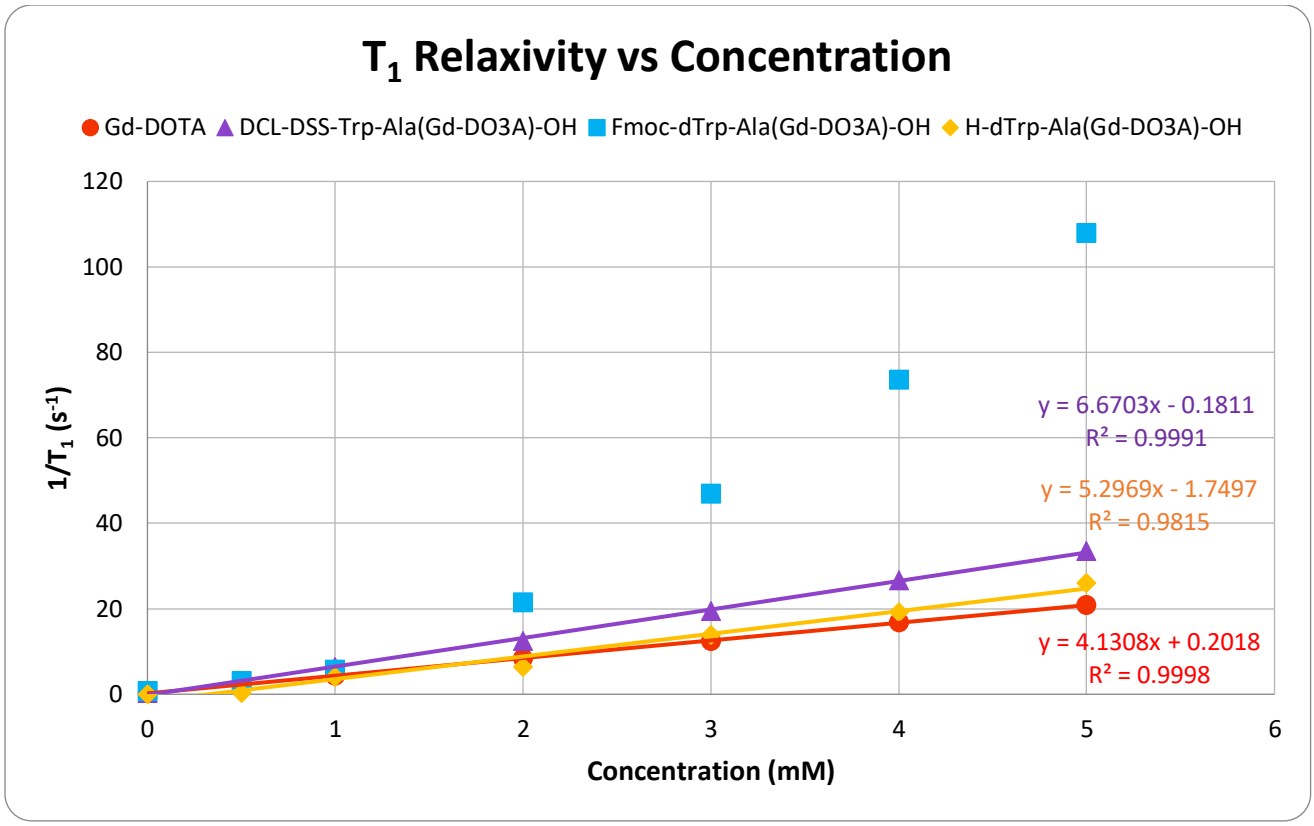

Figure 25: (Above) T_1 relaxivities of Gd-DOTA (red), Fmoc-dTrp-Ala(Gd-DO3A)-OH (8) (blue), H-dTrp-Ala(Gd-DO3A)-OH (9) (yellow), and DCL-DSS-dTrp-Ala(Gd-DO3A)-OH (10) (purple), plotted against concentration (mM) in water as measured with a 43 MHz Magritek NMR. Nonlinearity of Fmoc-dTrp-Ala(Gd-DO3A)-OH does not lend itself to trendline plotting and therefore relaxivity cannot not be reported.

To ensure the results, the sample was re-purified, re-freeze dried and the solutions were prepared a second time by Andrew O'Brien, who was following up on this finding, with nearly identical results. (**Fig. 26**) While the reasons for this increase in relaxivity at the higher concentrations are not entirely clear at this time, there are a few speculations that we can make.

First, Gd^{3+} when not in chelation has a very high T_1 relaxivity. There is a possibility of Gd partially dissociating from its coordination complex as the concentration of the CA increases. This would be observed as a non-linear increase in relaxivity as concentration increases. However, when the sample was retrieved and tested by LC-MS, no de-metallation had resulted. Furthermore, if demetallation were occurring, we think similar non-linear increases would also be seen in the other complexes containing Trp-Ala(Gd-DO3A)-OH as well, but this was not observed in the data points of the other compounds which followed a linear trend.

In another aspect, it is important to recognize that this unusual effect with high relaxivity at higher concentrations, and with normal relaxivity at lower concentrations only occurred in the one case where two aromatic ring systems were in proximity to each other. The examples where the single tryptophan or single fluorine group were present did not yield this effect. We therefore speculate further that the curve might be bi-phasic (as shown in **Figure 26**) due to an effect such as aggregation caused by pi-stacking which requires the presence of at least two aromatic rings.[48] However, such speculation clearly requires more data points from this compound, and additional results from additional compounds in order to firm up the theory.

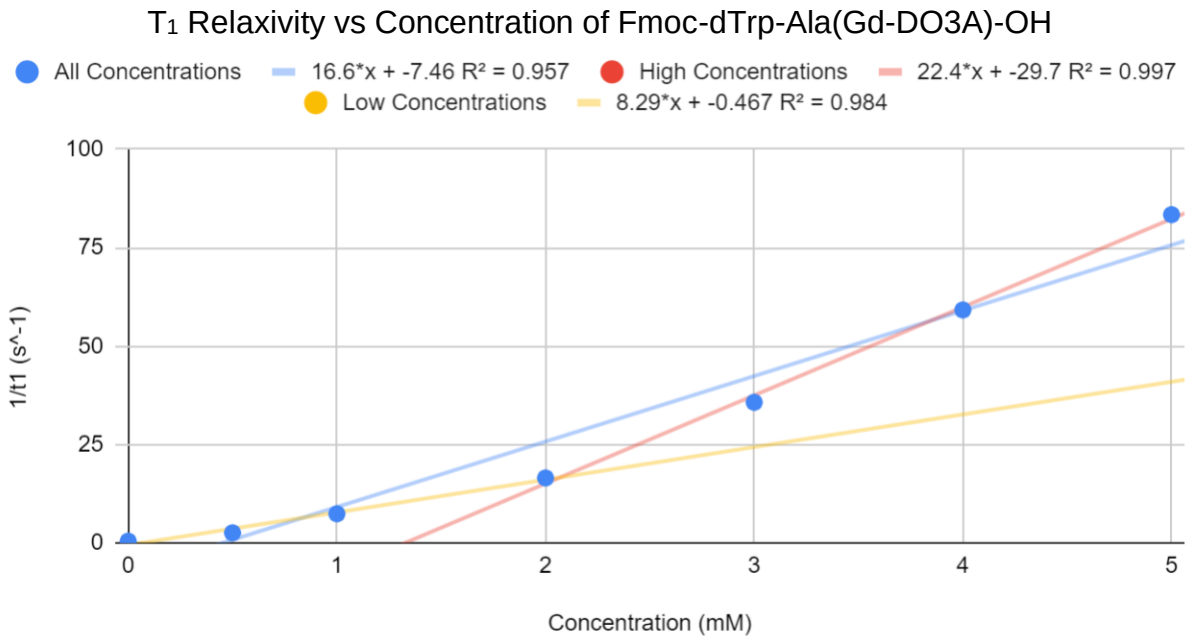

Figure 26: (Above) Third set of T_1 relaxivity data of F-dTrp-Ala(Gd-DO3A)-OH (**8**) where r1 = 16.63 ± 3.08 $mM^{-1}s^{-1}$. (Data was acquired by Andrew O'Brien.)

In summary, while the exact mechanism and factors which give rise to this non-linear trend are not clear, this unexpected finding represents an opportunity for future students to investigate the origin of the effect and possibly exploit in developing a method to prepare true high-relaxivity agents across all concentrations. It can be said, however, that a high relaxivity agent has been prepared in compound **8**, though only at concentrations above 2 mM, and lays the groundwork for future advances in the design of high-relaxivity agents for MRI.

Conclusions

A new method for the synthesis of high-relaxivity compounds based on the alanine approach by Boros has been developed.[35] The result is a total synthesis of the targeted molecular imaging agent (TMIA), also called high relaxivity targeted contrast agent (HR-TCA) from a readily purchased precursor, Cbz-Ser(H)-OBn. The modular approach dispenses with the t-butyl protecting groups described in the literature and replaces them with the Gd metal which also serves as a protecting group in addition to its role as a contrast agent.

The synthesis involves the further insertion of tryptophan to add lipophilicity, a UV handle for use in diode array detection, to slow down the compound on C18 silica during purification, to increase bioavailability and cell permeation and, as hypothesized, to boost the T_1 relaxivity. In the final steps, the resulting imaging module H-Trp-Ala(Gd-DO3A)-OH is coupled in a convergent step with the targeting module DCL-DSS to afford the final HR-TCA, DCL-DSS-Trp-Ala(Gd-DO3A)-OH (10).

While the measured T_1 relaxivity of the final HR-TCA DCL-DSS-Trp-Ala(Gd-DO3A)-OH (10) was somewhat disappointing as it was not quite high enough to firmly be considered high-relaxivity, the successful synthesis of imaging module H-Trp-Ala(Gd-DO3A)-OH (9) could still provide high relaxivity in agents that contained additional structural features which we hypothesize were present in the larger peptides prepared by Boros, et al.[35] As the prior literature clearly indicates that Ala(Gd-DO3A) can provide high relaxivity in larger peptides, our synthesis, which involved extensive optimization of each step, paves the way for its incorporation into future TMIAs.

In a surprising finding, it was discovered that the intermediate, Fmoc-dTrp-Ala(Gd-DO3A)-OH (8) did exhibit high T_1 relaxivity in our measurements. It is hypothesized that the addition of aromatic moieties, such as an extra aromatic residue or Fmoc group on an adjacent amino acid, that such structural modifications could indeed lead to CAs of much higher T_1 relaxivity. Thus, this presents an opportunity for future students to investigate the exact mechanisms and factors responsible this trend in our data, and to further develop true high-relaxivity agents for MRI.

Experimental Procedures

General Considerations

Chemicals were HPLC or American Chemical Society grade and were purchased from VWR (Radnor, PA), Sigma Aldrich (St. Louis, MO), Alfa Aesar (Ward Hill, MA), TCI (Tokyo, Japan), and Acros Organics (Morris Plains, NY), and, unless stated otherwise, were used as received. Amino acid starting materials were purchased from Bachem (Bubendorf, Switzerland), and Ambeed. (Arlington Heights, IL). DOTA was purchased from Macrocyclics (Houston, TX).

The HPLC-MS instrument used was a Waters 2695 Alliance HPLC with a Waters 2998 Diode Array Detector and a Waters 3100 SQ Mass Spectrometer. HPLC columns used were an Agilent XDB C18 column (3 mm x 100 mm, 3μ) and a Waters XBridge C18 column (50 mm x 3 mm, 3μ). Mass spectra were recorded at unit resolution with positive and negative switching mode at 35 V cone voltages. HPLC was configured with 0.5 mL/min flow rate and solvent system of ACN in 0.1 M ammonium acetate aqueous phase.

Flash HPLC instrument was run on a Biotage Selekt with a Biotage Sfär C18 30g column, configured with a flow rate of 25 mL/min, and fraction collection volume of 20 mL. Fractions were collected in 16 x 150 mm test tubes.

Data for high resolution mass spectra (HRMS) was outsourced to the School of Chemical Sciences at the University of Illinois at Urbana-Champaign. Samples were run on a Waters Synapt G2Si using the following parameters: Flow injection at flow rate of 0.1 mL/min, H_2O/ACN/0.1% Formic Acid, positive and negative mode ESI, Cone voltage = 25, capillary voltage = 3.0, ion source temperature = - 100°C, desolation temperature = 180°C, nebulizing gas (N_2) flow = 200 L/h, cone gas (N2) flow = 5 L/h.

Cbz-Ser(Ms)-OBn (2)

Mesylation of the commercially available Cbz-Ser(H)-OBn starting material (1) (5.0 g, 15.18 μmol) was run for 30 minutes under argon gas at 0°C with Ms-Cl (1.2 eq) and TEA (1.6 eq) in DCM solvent. Crude reaction was extracted with DCM and deionized H_2O. Organic phase was rotary evaporated and dried with $MgSO_4$ overnight. The dried organic phase was filtered to remove the $MgSO_4$, dried *in vacuo*, then put under high vacuum overnight to obtain Cbz-Ser(Ms)-OBn (2) in excellent yield (>98%) and purity (>90%).

Cbz-Ala(Cyclen)-OBn (3)

Cbz-Ser(Ms)-OBn (2) (1.81 g, 4.44 μmol) was dissolved in ACN with 1.5 eq of K_2CO_3. The mixture was heated to 65°C and cyclen (4 eq) was added and allowed to react overnight. After filtering off the K_2CO_3 and concentrating the crude reaction *in vacuo*, a liquid-liquid back extraction was performed with EtOAC as the organic phase, two washes of deionized water, and a final wash with half saturated brine. The resulting washed organic phase was dried under $MgSO_4$ overnight, filtered, and then rotary evaporated to get rid of the bulk of the solvent. The remaining sticky residue was placed over high vacuum overnight. Cbz-Ala(Cyclen)-OBn (3) was obtained in 82% yield and approximately 85% purity.

Cbz-Ala(DO3A-tBu$_3$)-OBn (4)

Cbz-Ala(Cyclen)-OBn (3) (0.405 g, 8.4 μmol) was dissolved in acetone with K_2CO_3 (1.5 eq). Tert-butyl bromoacetate (3.2 eq) was added to the mixture and reacted for 16 hours at room temperature. Upon completion, the K_2CO_3 was filtered off and the remaining liquid was rotary evaporated as much as possible. The resulting residue underwent liquid-liquid extraction by dissolving it into EtOAc and washing once with deionized water followed by saturated brine. The organic layer was dried under $MgSO_4$ overnight, filtered, and rotary evaporated to remove all solvent. The thick, sticky residue was then dried over high vacuum overnight to afford Cbz-Ala(DO3A-*t*Bu$_3$)-OBn (4) at 75% yield and approximately 80% purity. LC-MS (LR, ESI) = Calcd. for $C_{44}H_{67}N_5O_{10}$ MW 827.05; Found 827.27 $[M+H]^+$.

Cbz-Ala(DO3A)-OBn (5)

Cbz-Ala(DO3A-*t*Bu$_3$)-OBn (4) (3.70 g, 44.82 μmol) was dissolved in pure TFA (25 mL), and TIPS (2 eq, 1.83 mL, 8.96 μmol) was immediately added as a radical scavenger before allowing to react for a maximum of 4-5 hours at room temperature. TFA was thoroughly removed *in vacuo* with multiple washes of ACN. The resulting residue, crude compound 5, was purified with reverse phase HPLC. Pure fractions were concentrated *in vacuo* and freeze dried overnight to obtain Cbz-Ala(DO3A)-OBn (5) at a final yields of 12.9-24.74% but near immaculate purity. LC-MS (LR, ESI) = Calcd. for $C_{32}H_{43}N_5O_{10}$ MW 658.73, Found 658.14 $[M+H]^+$. HRMS (HR, ESI) = 657.3010, Found 658.3090 $[M+H]^+$.

Cbz-Ala(Gd-DO3A)-OBn (6)

Cbz-Ala(DO3A)-OBn (5) (0.140 g, 0.64 μmol) was dissolved in 5 mL of 15% ACN in 5mM AmAc buffer and combined with 3 eq of $Gd(OAc)_3$ (0.214 g, 0.639 μmol). Mixture was allowed to stir for 15-30 min to obtain crude Cbz-Ala(Gd-DO3A)-OBn (6). Flash chromatography of crude compound 6 was run on C18 silica using gradients of ACN in 5mM AmAc buffer starting at 10% and increasing by increments of 10 up to 50%. The pure fractions were concentrated *in vacuo* and freeze dried overnight to afford purified compound 6. LC-MS (LR, ESI) = Calcd. for $C_{32}H_{40}GdN_5O_{10}$ MW 812.96, Found 813.03 $[M+H]^+$, 1217.96 $[3M+2H]^{2+}$, 1625.12 $[2M+H]^+$.

H-Ala(Gd-DO3A)-OH (7)

Cbz-Ala(Gd-DO3A)-OBn (6) (0.113 g, 0.139 μmol) was combined with Palladium Black (1 eq, 0.21 μmol) in methanol and allowed to react for 3 hours while H_2 gas was bubbled into the reaction. Filtration of as much catalyst as possible, concentration of the reaction *in vacuo,* and freeze drying the resulting residue yielded H-Ala(Gd-DO3A)-OH (7) at >100% yield. HRMS (HR, ESI) = Calcd. for $C_{17}H_{28}GdN_5O_8$ MW 586.6821, Found 587.11 $[M-H]^-$.

Fmoc-Trp-Ala(Gd-DO3A)-OH (8)

To synthesize Fmoc-Trp-Ala(Gd-DO3A)-OH (8), commercially available Fmoc-Trp-OH (1 eq, 0.0936 g, 0.159 μmol) was first activated with DIPEA (20 eq, 0.55 mL, 0.00318 μmol) and coupling agent TSTU (2 eq) in DMF solvent. In a separate flask, H-Ala(Gd-DO3A)-OH (7) was combined with just enough DMF to dissolve with 20 eq of DIPEA (0.55 mL, 0.00318 μmol). Prior combining the two mixtures, a small aliquot (~1-2 drops) of the activated Fmoc-Trp-Ala was crashed out of solution with diethyl ether, vortexed, and centrifuged. The supernatant was decanted while the remaining solids were dried under $Ar_{(g)}$ then combined with ~0.1% aqueous octylamine for HPLC to double check that the Fmoc-Trp-OH had properly been activated. Once activation of all Fmoc-Trp-OH was confirmed, the mixture of H-Ala(Gd-DO3A)-OH (7) and DIPEA was added and sealed under $Ar_{(g)}$ to react overnight in the fridge. Upon reaction completion, approximately half the DMF was removed *in vacuo* and combined diethyl ether to crash the product out of solution, vortexed, and then centrifuged. The supernatant was separated from the solids which were dried under $Ar_{(g)}$ to obtain crude Fmoc-Trp-Ala(Gd-DO3A)-OH (8). This was then put through C18 SPE with a gradient of 20%-50% ACN. The pure fractions were

collected, combined, and concentrated *in vacuo*, then freeze dried overnight to afford compound **8**, Fmoc-Trp-Ala(Gd-DO3A)-OH, at ~37% yield and ~75% purity. HRMS (HR, ESI) = Calcd. for $C_{43}H_{50}GdN_7O_{11}$ MW 995.1551, Found 995.2567 $[M-H]^-$.

H-Trp-Ala(Gd-DO3A)-OH (9)

Fmoc-Trp-Ala(Gd-DO3A)-OH (**8**) (0.0544 g, 0.055 μmol) was combined with 12.9 mL of DEA (24 eq, 1.311 μmol) in DMF and allowed to react for 2 hours. Upon completion, half of the solvent was removed *in vacuo*. The remaining residue was combined with diethyl ether to crash out the product which was then vortexed and centrifuged to separate the precipitate and supernatant. The precipitate was dried under $Ar_{(g)}$ to remove of any remaining diethyl ether and then dried under vacuum overnight to afford H-Trp-Ala(Gd-DO3A)-OH (**9**) at 77.78% yield. HRMS (HR, ESI) = Calcd. for $C_{28}H_{38}N_7O_9$ 773.1915 MW, Found 773.1897 $[M-H]^-$.

DCL-DSS-Trp-Ala(Gd-DO3A)-OH (10)

To synthesize DCL-DSS-Trp-Ala(Gd-DO3A)-OH (**10**), H-Trp-Ala(Gd-DO3A)-OH (**9**) (0.010 g, 0.011 μmol) was combined with TEA (16 eq) in DMF. Once dissolved, in-house made targeting group with attached linker, DCL-DSS (1 eq, 0.0065 g, 0.011 μmol), was dissolved into the mixture. The reaction was sealed under $Ar_{(g)}$ and allowed to react overnight in the freezer. When completed, half of the DMF was removed *in vacuo* and product precipitated with diethyl ether. The mixture was then vortexed and centrifuged to remove the supernatant. The remaining precipitate was put through C18 SPE with 2%-30% Methanol gradient increasing in 2% increments. Pure fractions were combined and concentrated *in vacuo*, then freeze dried overnight to afford DCL-DSS-Trp-Ala(Gd-DO3A)-OH (**10**), the final HR-TCA, at 60.4% yield. LC-MS (LR, ESI) = 1232.39, Found 1231.88 $[M-H]^-$, 616.39 $[M+2H]^{2+}$. HRMS (HR, ESI) = Calcd. for $C_{48}H_{69}GdN_{10}O_{18}$ MW 1230.3761, Found 1230.3960 $[M-H]^-$, 1212.3835 $[M-H_2O-H]^-$, 1252.3762 $[M+Na-2H]^-$.

Appendix I – HPLC-MS and HRMS Data

Compound **4**: Cbz-Ala(DO3A-tBu$_3$)-OBn

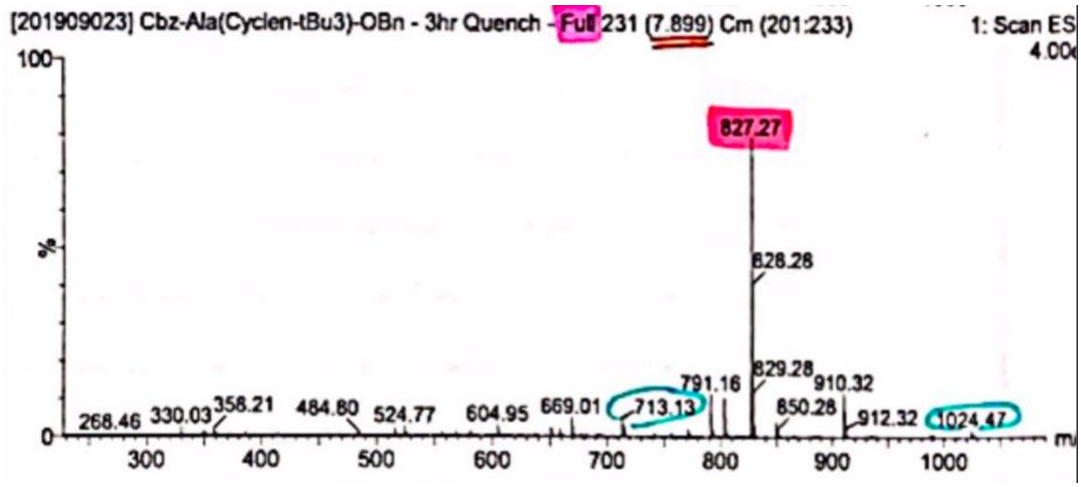

Positive ion LR mass spectra of Cbz-Ala(DO3A-tBu$_3$)-OBn (**4**) with parent ion $[M+H]^+$ at 827.27 m/z.

Compound *5*: Cbz-Ala(DO3A)-OBn

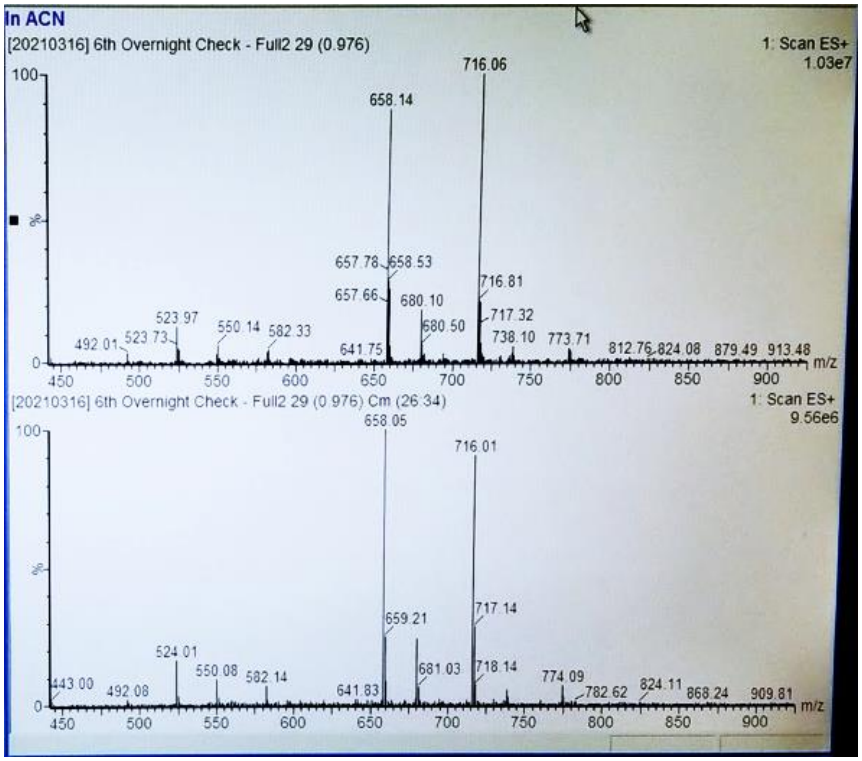

Positive ion mass spectra of Cbz-Ala(DO3A)-OH (*5*) (658.14 m/z) with acetal byproduct **4b** or hemiacetal byproduct **4c** (Scheme 3) at 716.06 m/z. A small peak representing the sodium adduct is seen at 680 m/z. Trace amounts of starting material where only one t-butyl has been removed can be seen at 773 m/z.

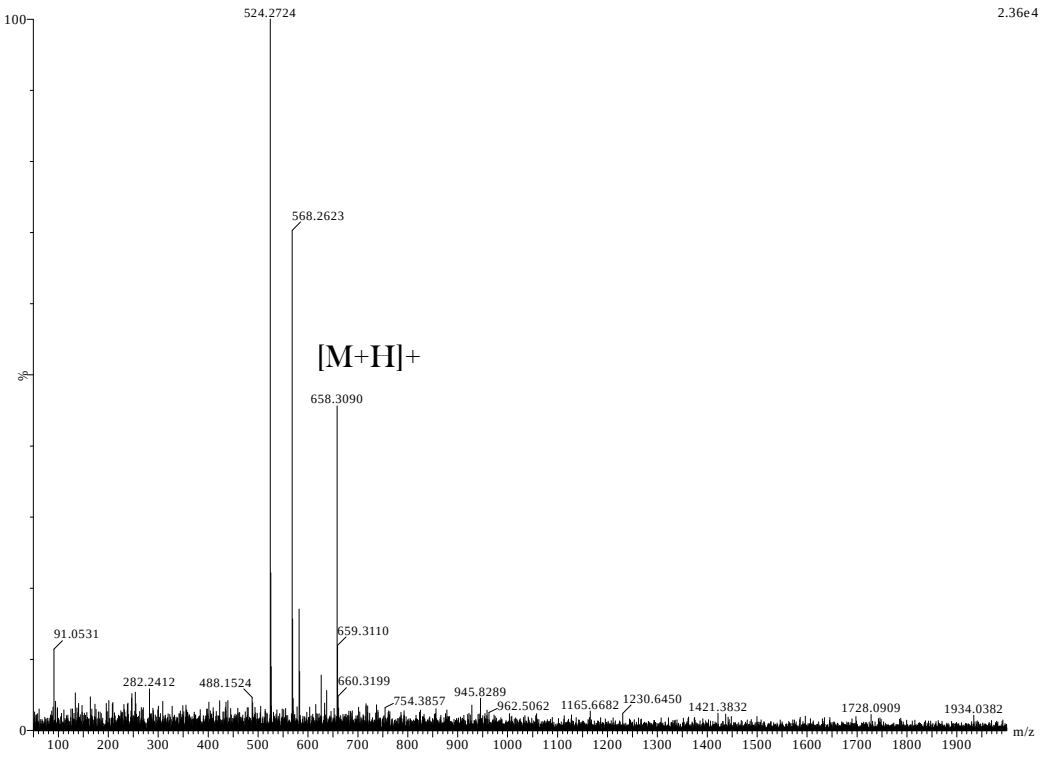

HRMS in positive ion mode of Cbz-Ala(DO3A)-OH (*5*) (658.3090 m/z). Mass at 568.2623 m/z is speculated to be fragmentation loss of the Bn protecting group, and 524.2724 m/z is speculated to be further loss of carbon dioxide from the C-terminal backbone in the instrument.

Compound 6: Cbz-Ala(Gd-DO3A)-OBn

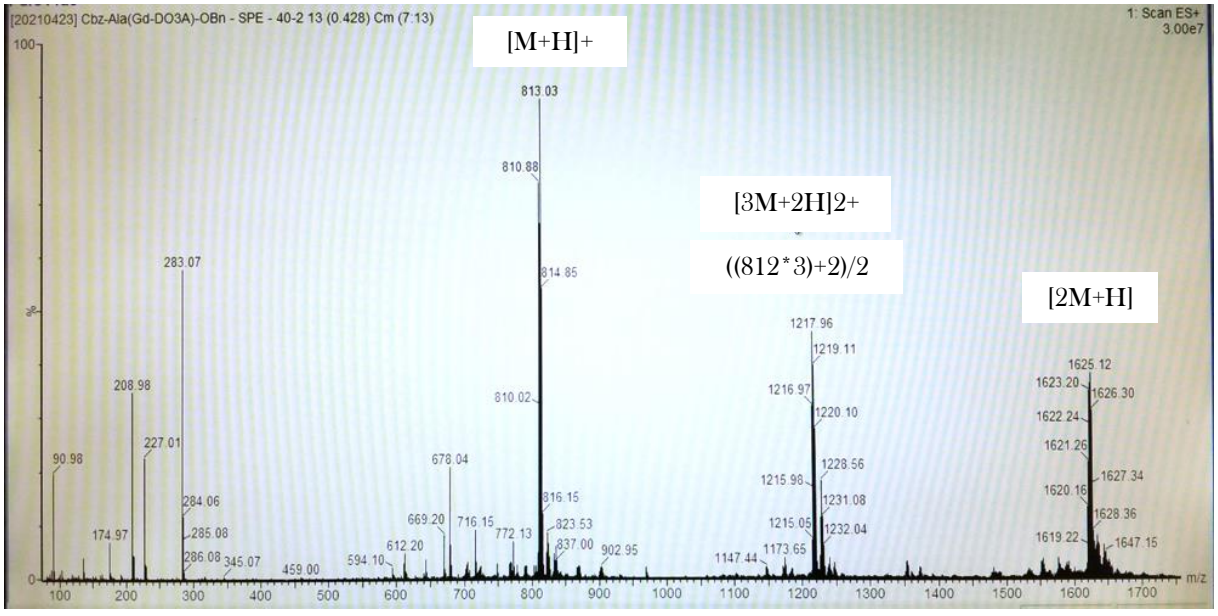

Positive ion LR mass spectra of a fraction from the reverse phase SPE purification Cbz-Ala(Gd-DO3A)-OBn (**6**) (813.03 m/z). Multiply charged cluster $[3M+2H]^{2+}$ can be seen at 1217.96 m/z, as well as the mass spec dimer $[2M+H]^{+}$ at 1625.12 m/z.

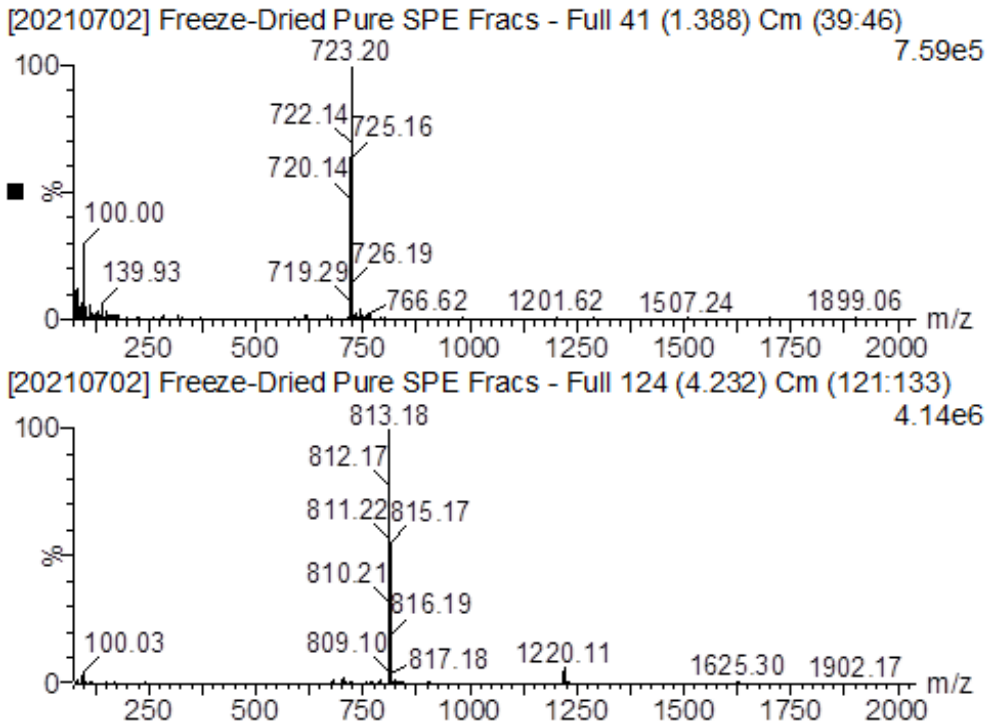

Positive ion LR mass spectra of the peaks at 1.39 (top) and 4.23 (bottom) retention time showing the hydrolyzed product (723.20 m/z, loss of benzyl) and Cbz-Ala(Gd-DO3A)-OBn (6) (813.18 m/z), respectively.

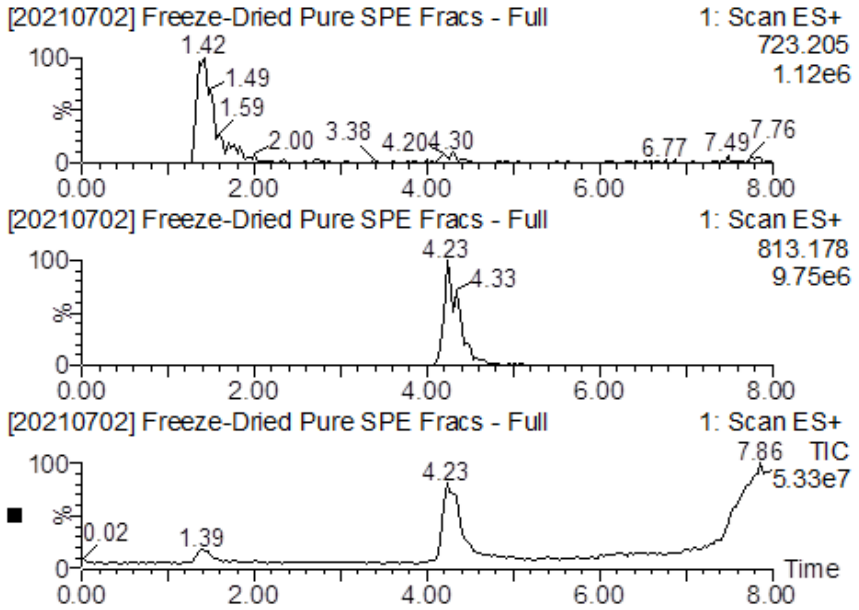

Extracted positive ion chromatograms of compound 6 where the Bn protecting group has been hydrolyzed to form Cbz-Ala(Gd-DO3A)-OH (top) and full in-tact product (middle) alongside the total ion chromatogram (bottom). Difference in retention time suggests the hydrolytic cleavage of Bn occurs outside the mass spectrometer and is therefore not the result of a fragmentation reaction inside the instrument.

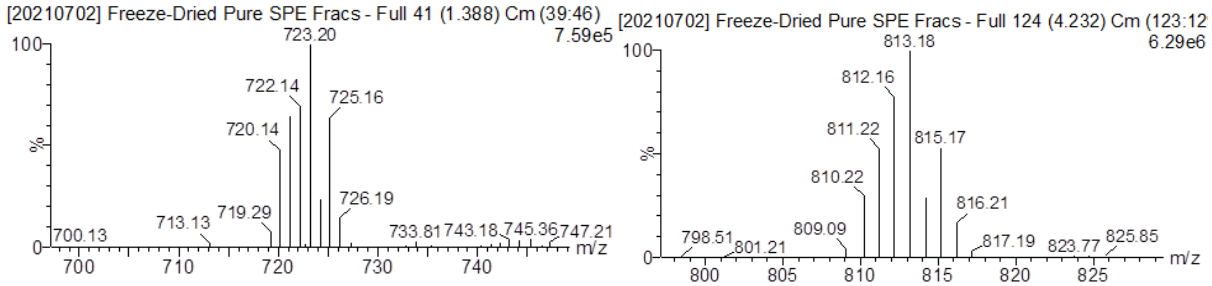

Gd isotope patterns of the hydrolyzed Cbz-Ala(Gd-DO3A)-OH (6) (left) and full intact product (right) confirming presence of Gd in the final, freeze-dried materials.

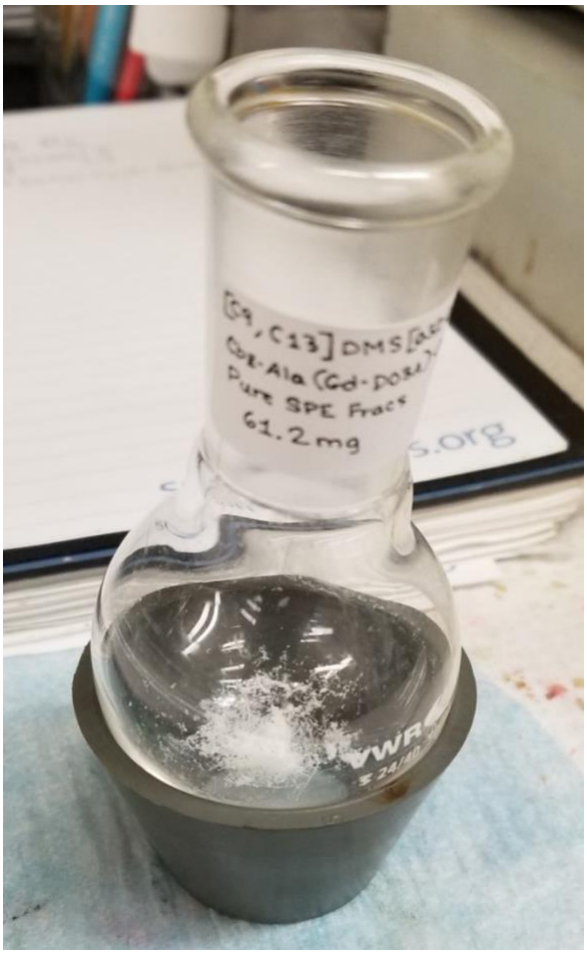

Purified Hydrolyzed Cbz-Ala(Gd-DO3A)-OBn (6) appears as white tiny crystals.

Compound **7**: H-Ala(Gd-DO3A)-OH

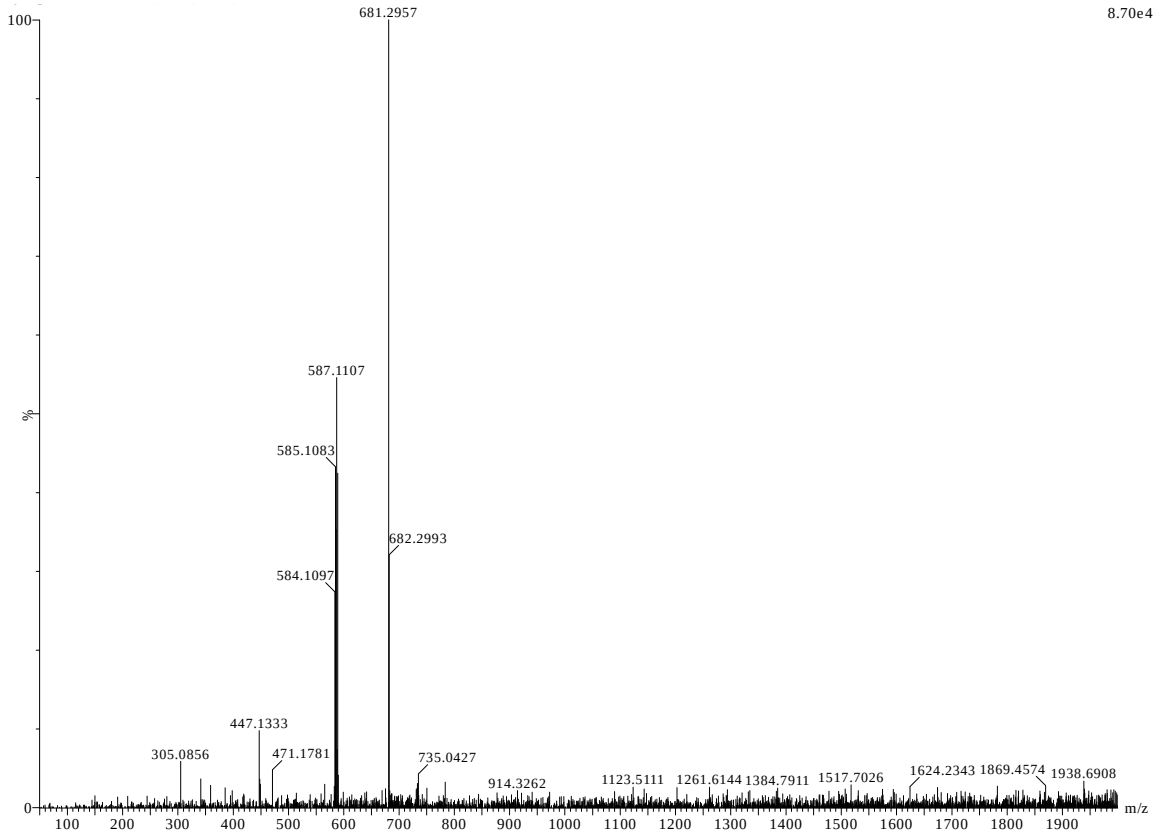

HRMS in negative ionization mode of H-Ala(Gd-DO3A)-OH (**7**) at 587.1107 m/z.

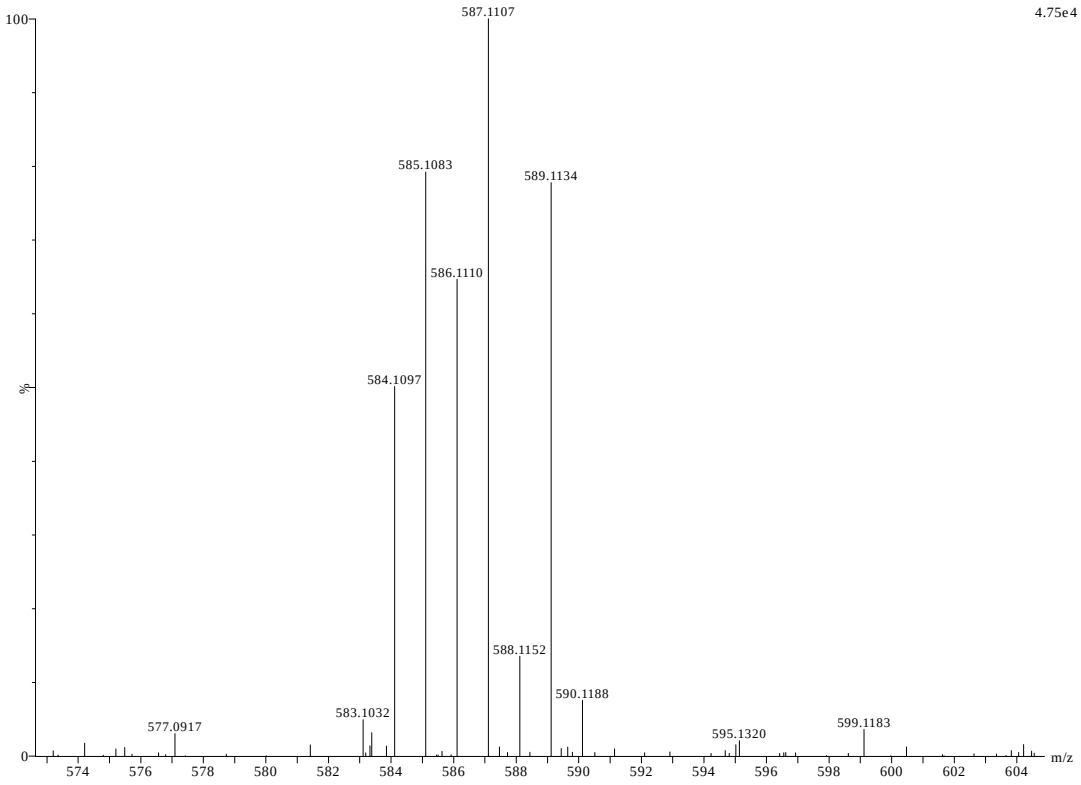

Gd Isotope pattern in negative ion mode of high-resolution mass spectra of H-Ala(Gd-DO3A)-OH (**7**).

Compound 8: Fmoc-dTrp-Ala(Gd-DO3A)-OH

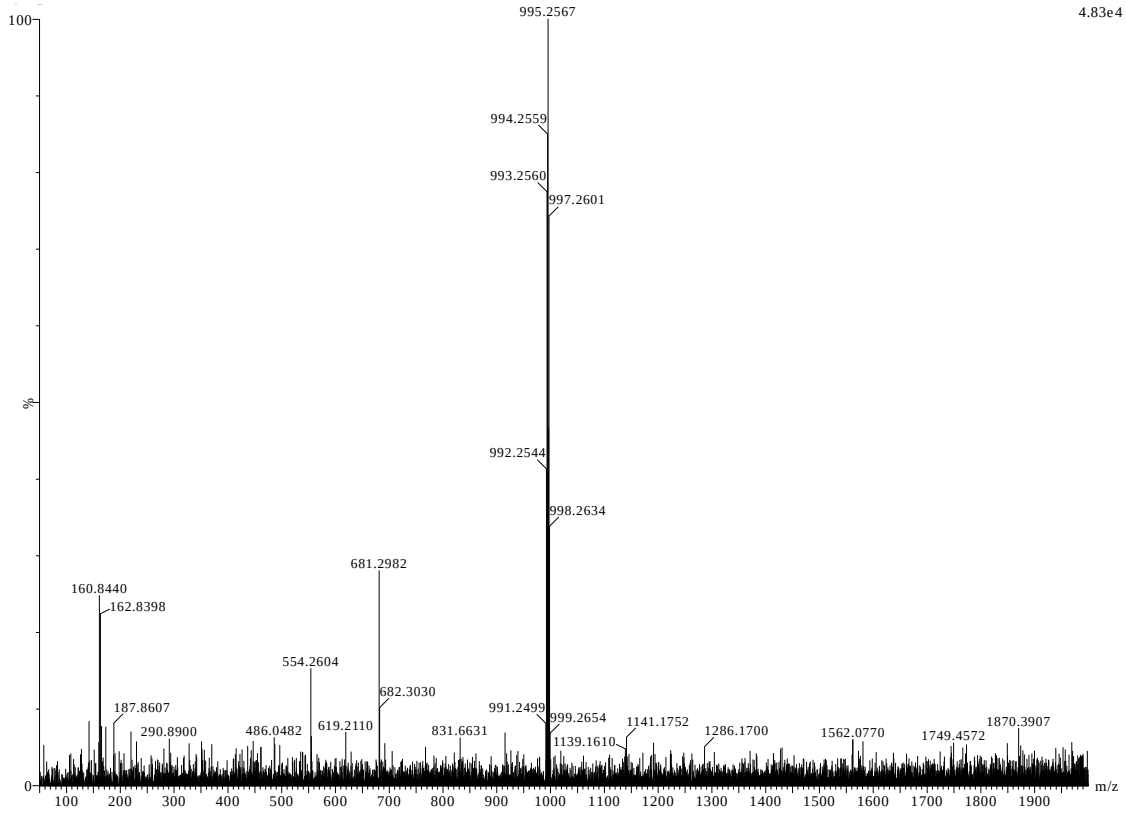

HRMS in negative ionization mode of Fmoc-dTrp-Ala(Gd-DO3A)-OH (**8**) (995.2567 m/z).

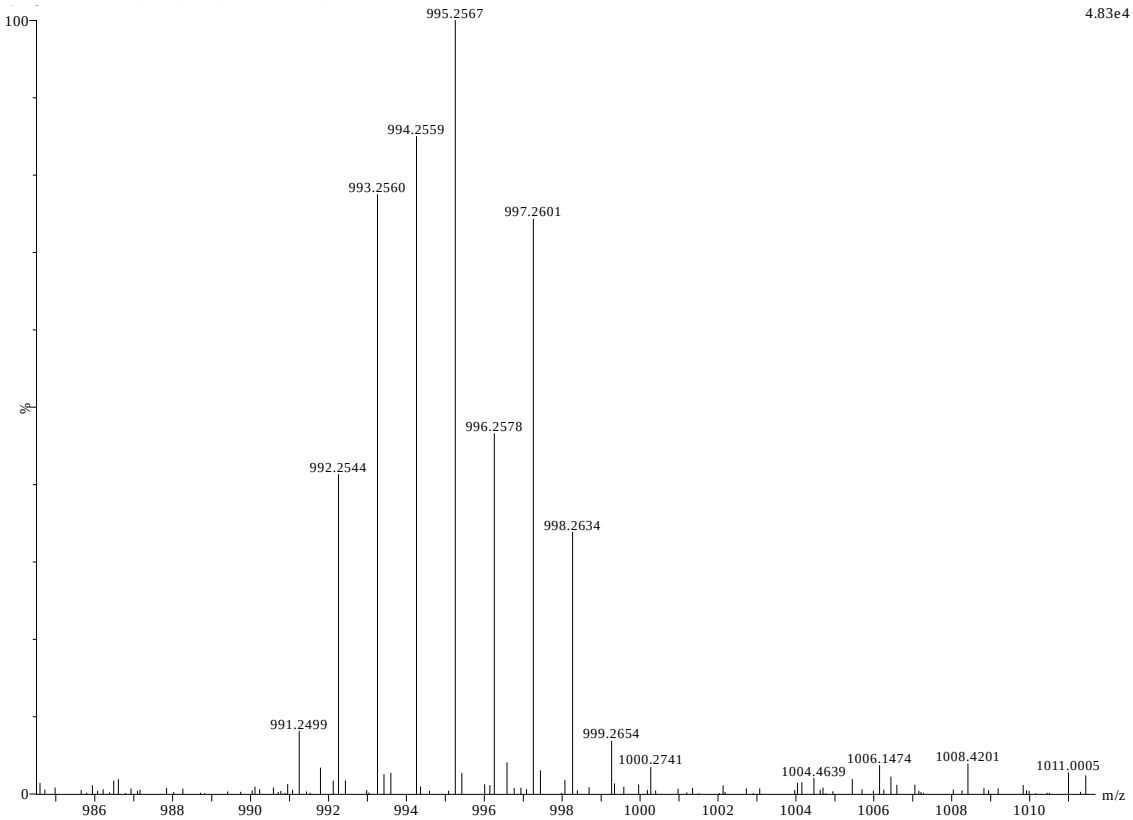

Gd isotope pattern in negative ion mode of high-resolution mass spectra of Fmoc-dTrp-Ala(Gd-DO3A)-OH (**8**).

Compound 9: H-dTrp-Ala(Gd-DO3A)-OH

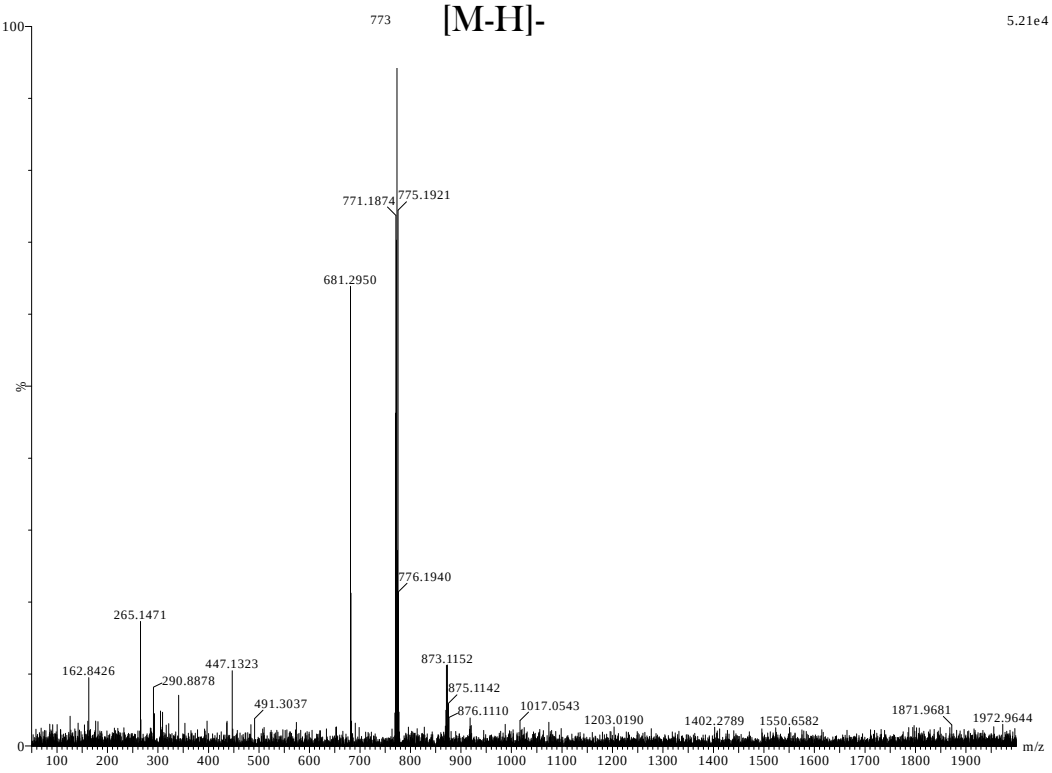

HRMS in negative ionization mode of H-dTrp-Ala(Gd-DO3A)-OH (**9**) (773.1897 m/z) in negative ion mode.

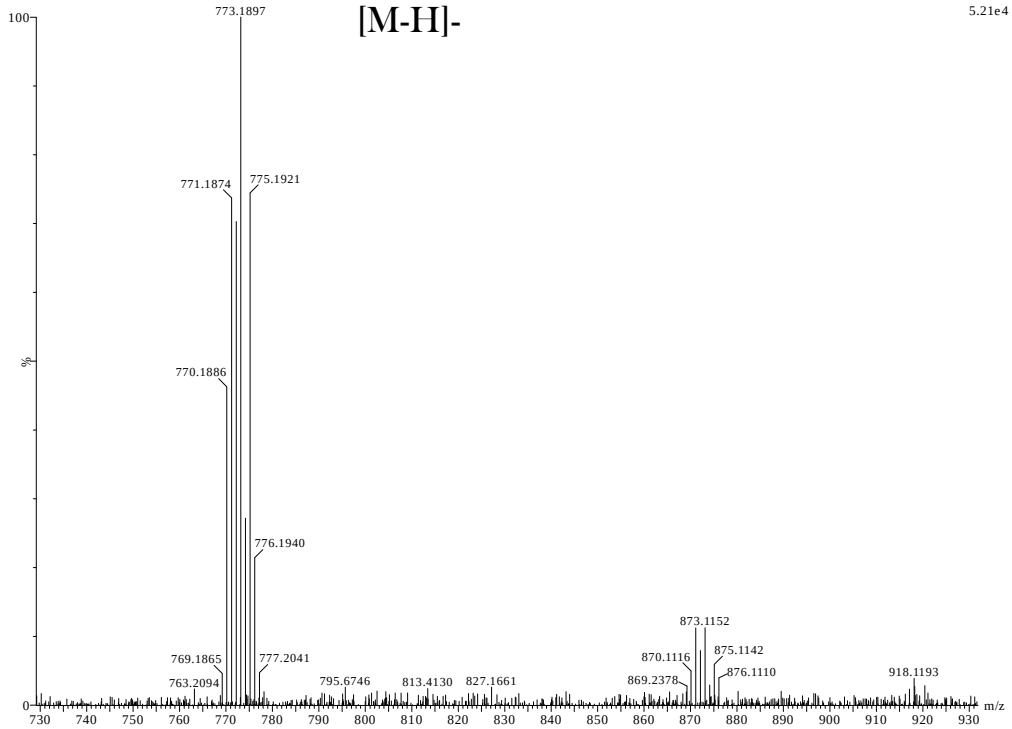

Gd isotope pattern of HRMS of H-dTrp-Ala(Gd-DO3A)-OH (**9**) in negative ion mode.

Compound 10: DCL-DSS-dTrp-Ala(Gd-DO3A)-OH

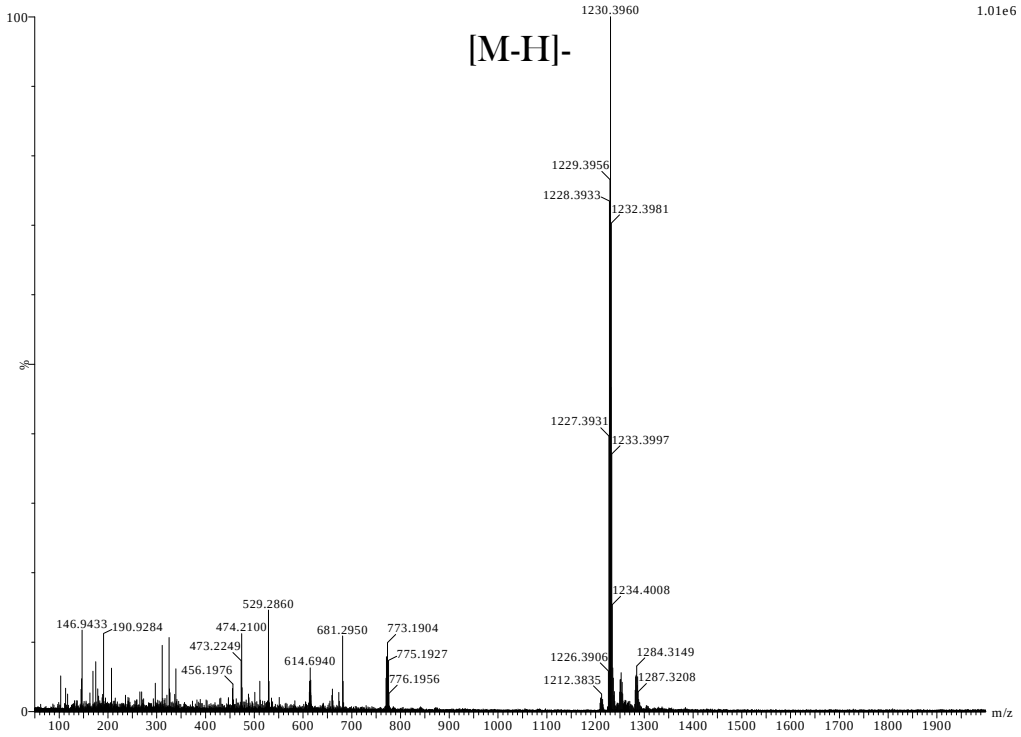

HRMS in negative ionization mode of DCL-DSS-dTrp-Ala(Gd-DO3A)-OH (**10**) (1230.3960 m/z).

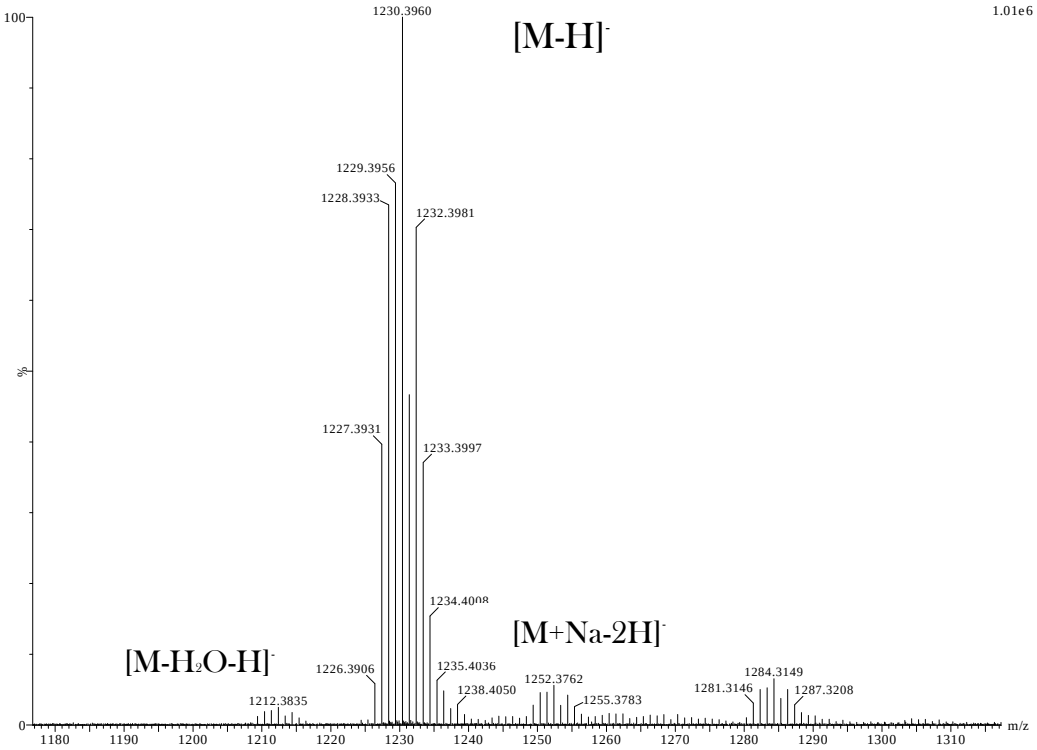

Isotope pattern in negative ion mode HRMS of DCL-DSS-dTrp-Ala(Gd-DO3A)-OH (**10**).

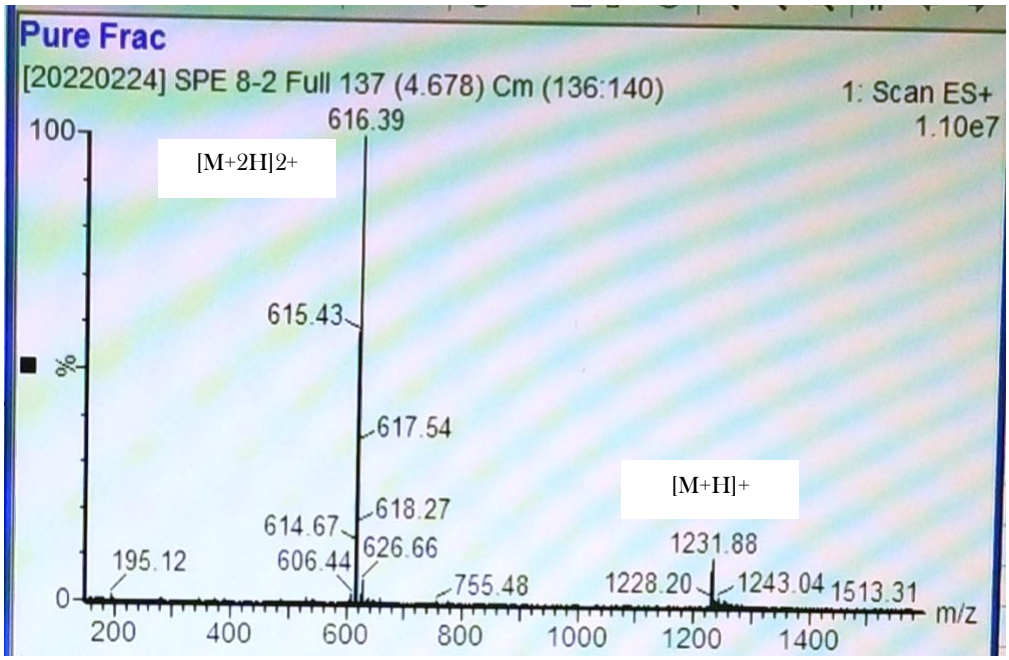

Positive ion LR mass spectra of pure fraction from SPE purification of DCL-DSS-dTrp-Ala(Gd-DO3A)-OH (**10**). Both the full and half mass can be seen at 1231.88 m/z and 616.39 m/z, respectively.

DCL-DSS-dTrp-Ala(Gd-DO3A)-OH (**10**) freeze drying on a vacuum manifold.

DSS-Trp-Ala(Gd-DO3A)-OH

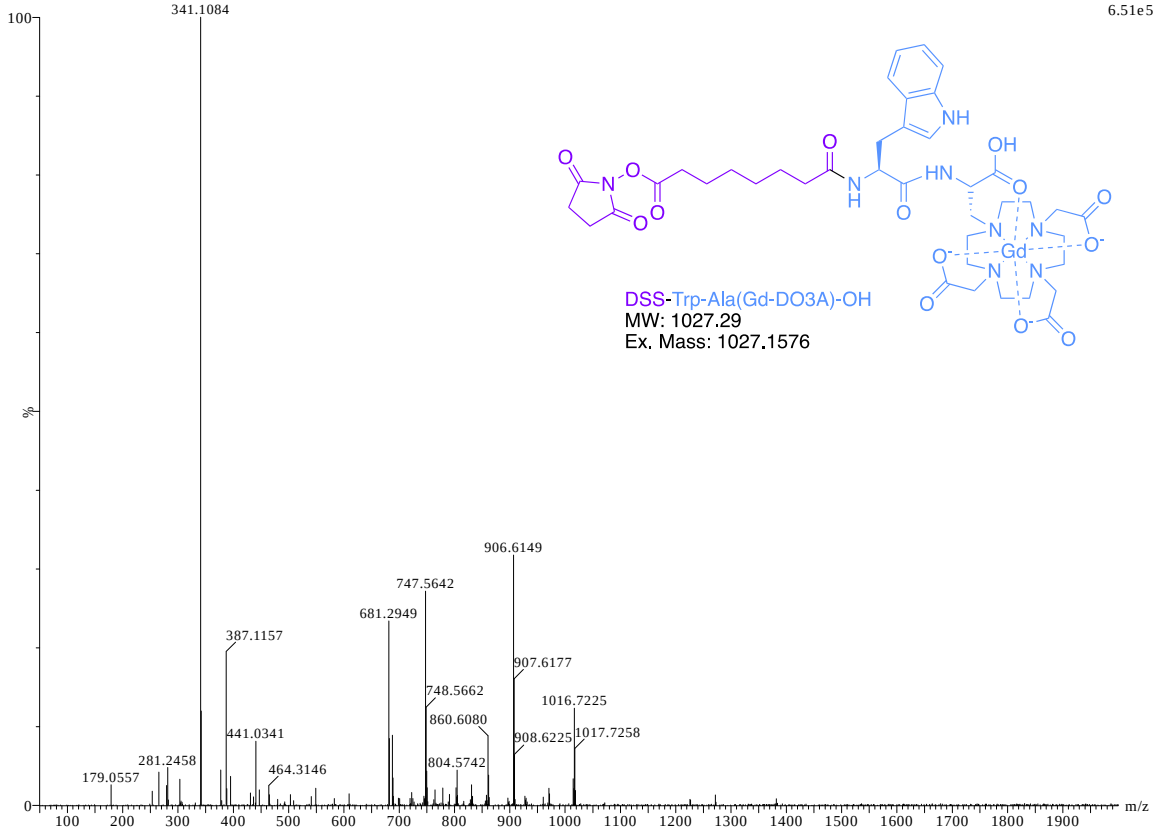

HRMS of alternative synthetic route intermediate DSS-Trp-Ala(Gd-DO3A)-OH in negative ion mode.

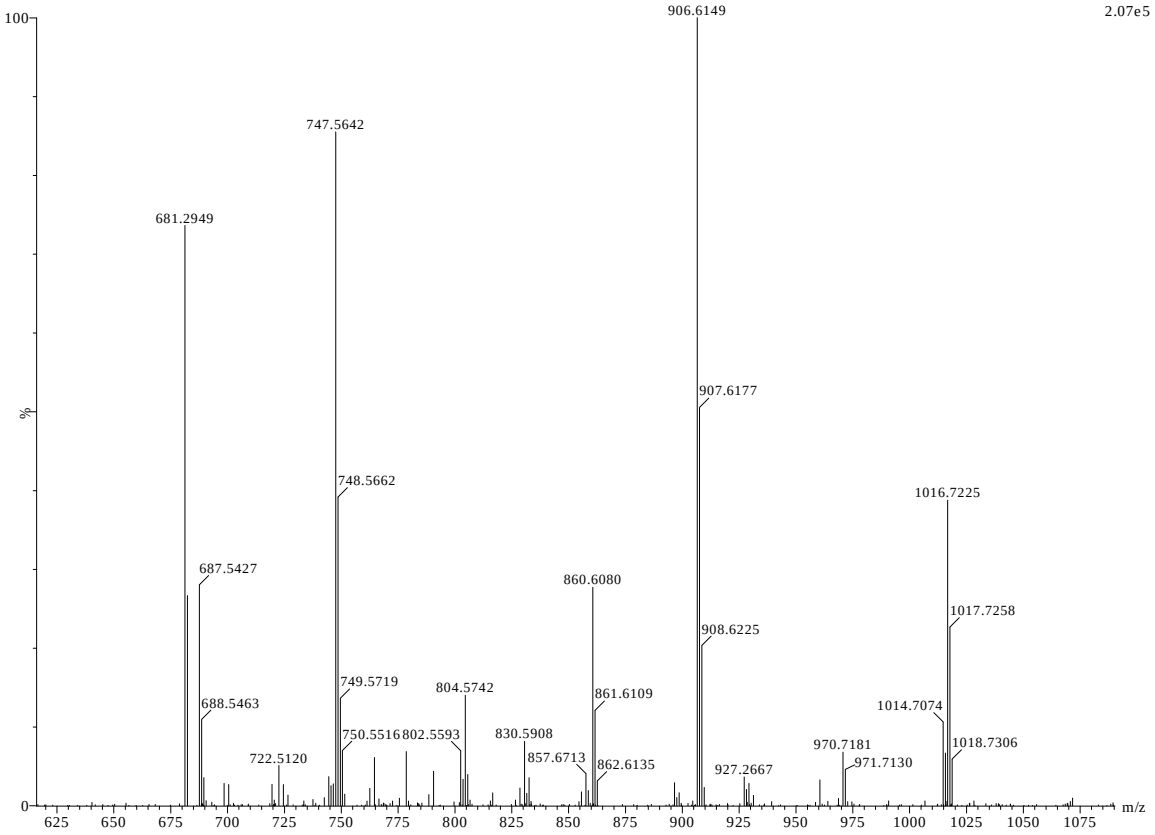

Zoomed in HRMS of alternative synthetic route intermediate DSS-Trp-Ala(Gd-DO3A)-OH in negative ion mode.

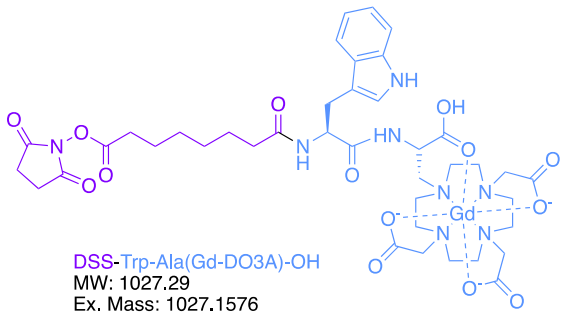

T_1 Relaxivity Data

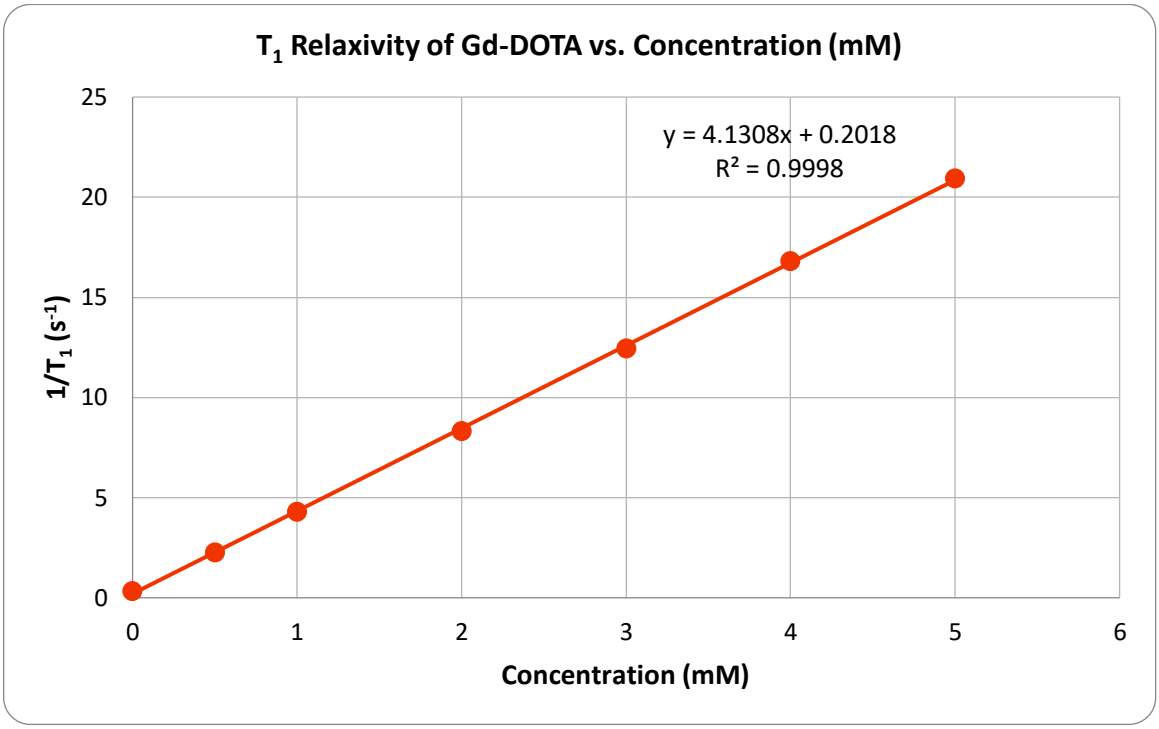

T_1 relaxivity of Gd-DOTA plotted against concentration (mM). Gd-DOTA r_1 = 4.1308 $mM^{-1}s^{-1}$.

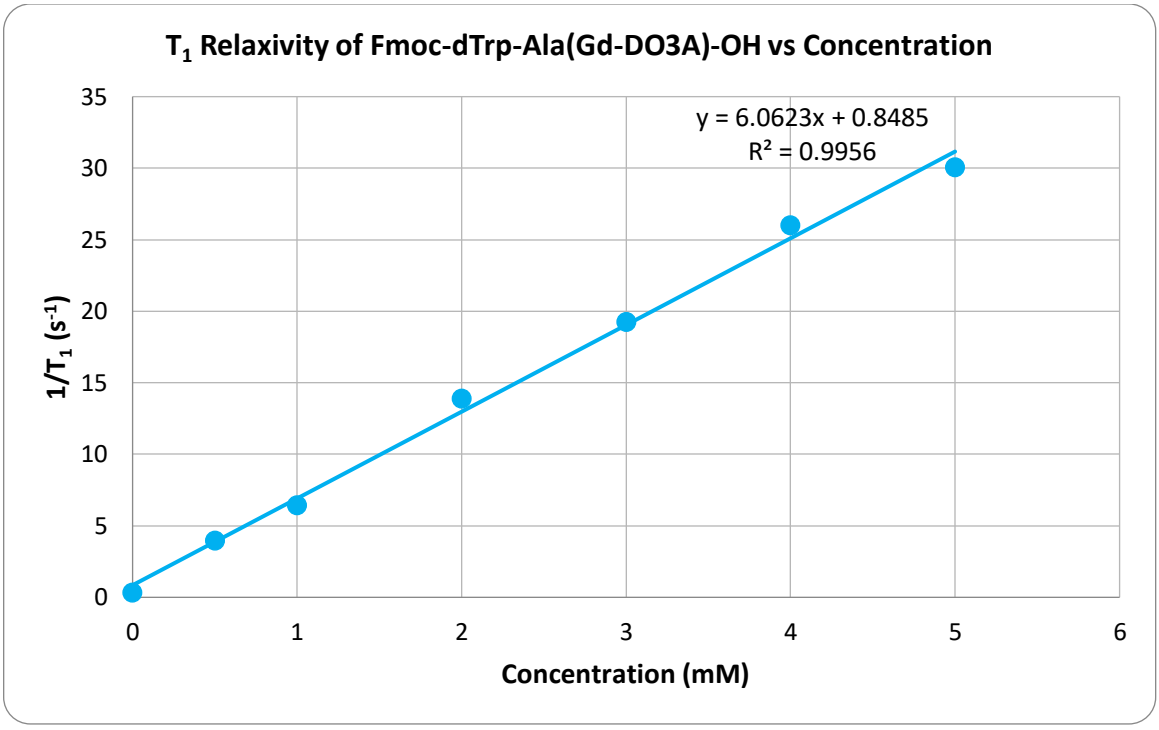

T_1 relaxivity of Fmoc-dTrp-Ala(Gd-DO3A)-OH (**8**) plotted against concentration (mM). Fmoc-dTrp-Ala(Gd-DO3A)-OH (**8**) was found to have a relaxivity value of 21.528 $mM^{-1}s^{-1}$.

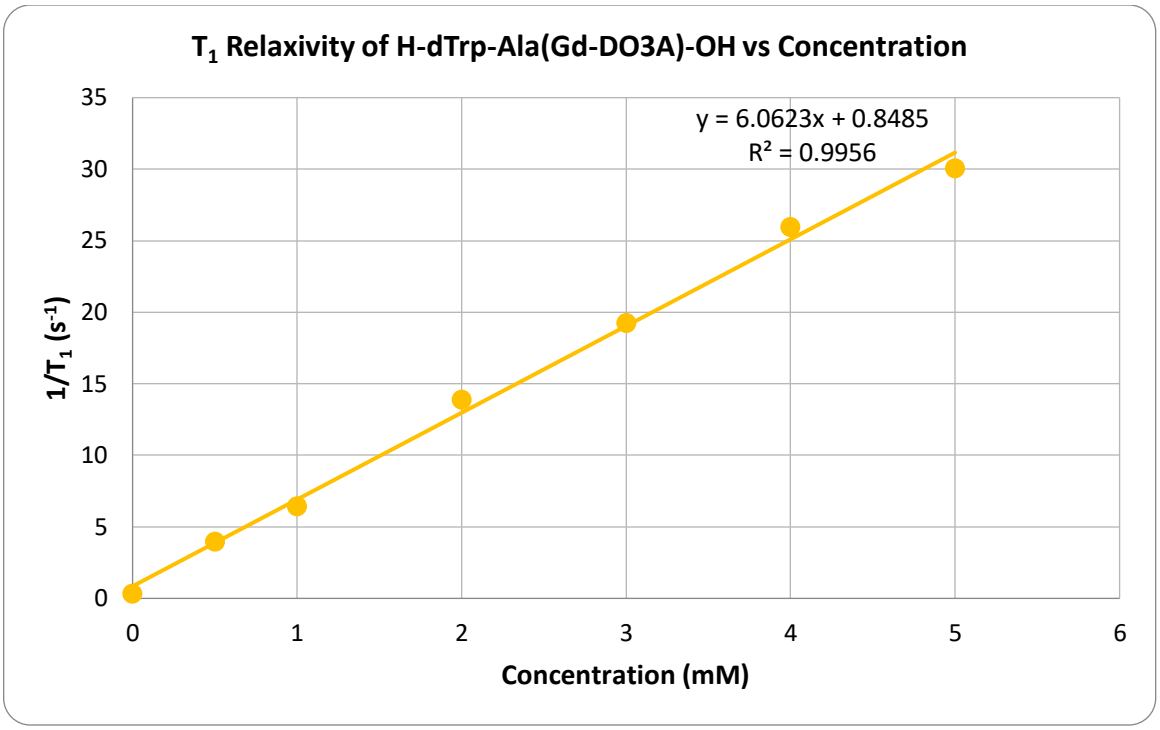

T_1 relaxivity of H-dTrp-Ala(Gd-DO3A)-OH (**9**) plotted against concentration (mM) was 6.0623 $mM^{-1}s^{-1}$.

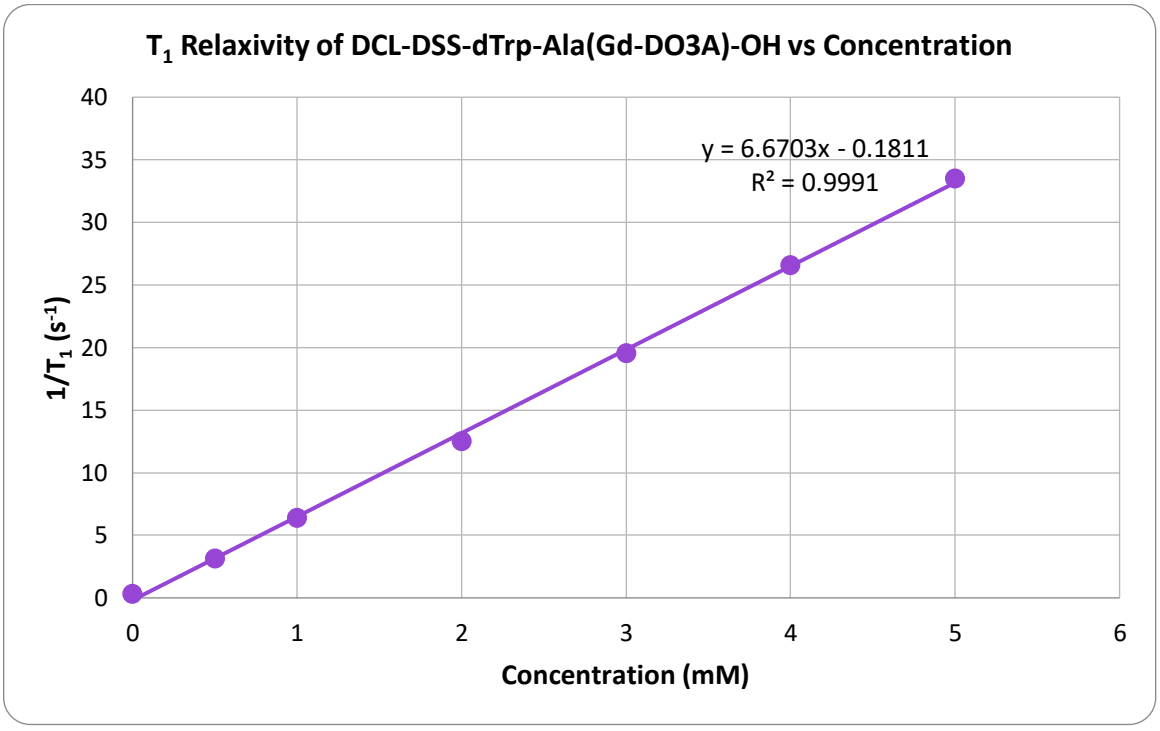

T_1 relaxivity of DCL-DSS-dTrp-Ala(Gd-DO3A)-OH (**10**) plotted against concentration (mM) as measured with 43 MHz Magritek NMR Spectrometer. DCL-DSS-dTrp-Ala(Gd-DO3A)-OH (**10**) was found to have a T_1 relaxivity value of 6.6703 $mM^{-1}s^{-1}$.

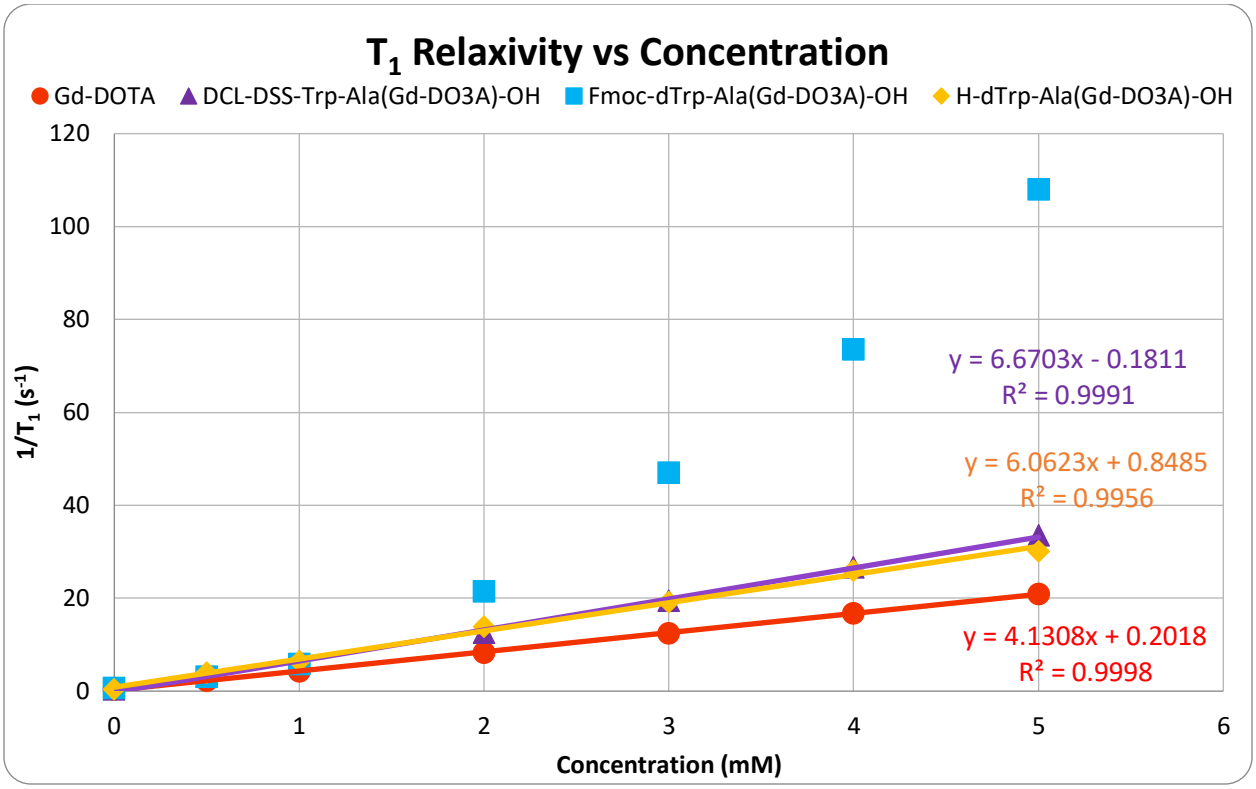

T_1 relaxivities of Gd-DOTA (red), Fmoc-dTrp-Ala(Gd-DO3A)-OH (**8**) (blue), H-dTrp-Ala(Gd-DO3A)-OH (**9**) (gold), and DCL-DSS-Trp-Ala(Gd-DO3A)-OH (**10**) (purple), plotted against concentration (mM) as measured with a 43 MHz Magritek NMR.

References

(1) *The Cancer Atlas*. The Cancer Atlas. http://canceratlas.cancer.org/33i (accessed 2020-07-23).
(2) *FastStats*. https://www.cdc.gov/nchs/fastats/leading-causes-of-death.htm (accessed 2020-07-23).
(3) *Cancer Facts & Figures 2022| American Cancer Society*. https://www.cancer.org/research/cancer-facts-statistics/all-cancer-facts-figures/cancer-facts-figures-2022.html (accessed 2022-08-19).
(4) *Key Statistics for Prostate Cancer | Prostate Cancer Facts*. https://www.cancer.org/cancer/prostate-cancer/about/key-statistics.html (accessed 2022-08-19).
(5) *Cancer Statistics - National Cancer Institute*. https://www.cancer.gov/about-cancer/understanding/statistics (accessed 2020-08-05).
(6) Weir, H. K. Cancer Incidence Projections in the United States Between 2015 and 2050. *Prev. Chronic Dis.* **2021**, *18*. https://doi.org/10.5888/pcd18.210006.
(7) Bracken, C. P.; Scott, H. S.; Goodall, G. J. A Network-Biology Perspective of MicroRNA Function and Dysfunction in Cancer. *Nature Reviews Genetics* **2016**, *17* (12), 719–732. https://doi.org/10.1038/nrg.2016.134.
(8) Brock, M. V.; Hooker, C. M.; Ota-Machida, E.; Han, Y.; Guo, M.; Ames, S.; Glöckner, S.; Piantadosi, S.; Gabrielson, E.; Pridham, G.; Pelosky, K.; Belinsky, S. A.; Yang, S. C.; Baylin, S. B.; Herman, J. G. DNA Methylation Markers and Early Recurrence in Stage I Lung Cancer. *New England Journal of Medicine* **2008**, *358* (11), 1118–1128. https://doi.org/10.1056/nejmoa0706550.
(9) Fitzsimmons, C. M.; Batista, P. J. It's Complicated... M6A-Dependent Regulation of Gene Expression in Cancer. *Biochimica et Biophysica Acta (BBA) - Gene Regulatory Mechanisms* **2019**, *1862* (3), 382–393. https://doi.org/10.1016/j.bbagrm.2018.09.010.
(10) Fan, Y.; Dutta, J.; Gupta, N.; Fan, G.; Gélinas, C. Regulation of Programmed Cell Death by NF-KB and Its Role in Tumorigenesis and Therapy. In *Programmed Cell Death in Cancer Progression and Therapy*; Khosravi-Far, R., White, E., Eds.; Advances in Experimental Medicine and Biology; Springer Netherlands: Dordrecht, 2008; pp 223–250. https://doi.org/10.1007/978-1-4020-6554-5_11.
(11) Barrett, T.; Haider, M. A. The Emerging Role of MRI in Prostate Cancer Active Surveillance and Ongoing Challenges. *American Journal of Roentgenology* **2016**, *208* (1), 131–139. https://doi.org/10.2214/AJR.16.16355.
(12) Michalski, M. H.; Chen, X. Molecular Imaging in Cancer Treatment. *European Journal of Nuclear Medicine and Molecular Imaging; Heidelberg* **2011**, *38* (2), 358–377. http://dx.doi.org/10.1007/s00259-010-1569-z.
(13) Boros, E.; M. Gale, E.; Caravan, P. MR Imaging Probes: Design and Applications. *Dalton Transactions* **2015**, *44* (11), 4804–4818. https://doi.org/10.1039/C4DT02958E.
(14) Arvelo, F.; Sojo, F.; Cotte, C. Tumour Progression and Metastasis. *Ecancermedicalscience* **2016**, *10*. https://doi.org/10.3332/ecancer.2016.617.
(15) Klein, C. A. Parallel Progression of Primary Tumours and Metastases. *Nature Reviews. Cancer; London* **2009**, *9* (4), 302–312. http://dx.doi.org/10.1038/nrc2627.
(16) Dregely, I.; Prezzi, D.; Kelly-Morland, C.; Roccia, E.; Neji, R.; Goh, V. Imaging Biomarkers in Oncology: Basics and Application to MRI. *Journal of Magnetic Resonance Imaging* **2018**, *48* (1), 13–26. https://doi.org/10.1002/jmri.26058.
(17) Gonda, K.; Hamada, Y.; Kitamura, N.; Tada, H.; Miyashita, M.; Kamei, T.; Ishida, T.; Ohuchi, N. Highly Sensitive Imaging of Cancer with Functional Nanoparticles. *Journal of Photopolymer Science and Technology* **2015**, *28* (6), 731–736. https://doi.org/10.2494/photopolymer.28.731.
(18) Pavlícek, J.; Ptácek, J.; Barinka, C. Glutamate Carboxypeptidase II: An Overview of Structural Studies and Their Importance for Structure-Based Drug Design and Deciphering the Reaction Mechanism of the Enzyme. *Curr. Med. Chem.* **2012**, *19* (9), 1300–1309. https://doi.org/10.2174/092986712799462667.

(19) Mesters, J. R.; Barinka, C.; Li, W.; Tsukamoto, T.; Majer, P.; Slusher, B. S.; Konvalinka, J.; Hilgenfeld, R. Structure of Glutamate Carboxypeptidase II, a Drug Target in Neuronal Damage and Prostate Cancer. *EMBO J* **2006**, *25* (6), 1375–1384. https://doi.org/10.1038/sj.emboj.7600969.
(20) Davis, M. I.; Bennett, M. J.; Thomas, L. M.; Bjorkman, P. J. Crystal Structure of Prostate-Specific Membrane Antigen, a Tumor Marker and Peptidase. *Proc.Natl.Acad.Sci.USA* **2005**, *102*, 5981–5986. https://doi.org/10.2210/pdb1z8l/pdb.
(21) Pinto, J. T.; Suffoletto, B. P.; Berzin, T. M.; Qiao, C. H.; Lin, S.; Tong, W. P.; May, F.; Mukherjee, B.; Heston, W. D. Prostate-Specific Membrane Antigen: A Novel Folate Hydrolase in Human Prostatic Carcinoma Cells. *Clin Cancer Res* **1996**, *2* (9), 1445–1451.
(22) Machulkin, A. E.; Ivanenkov, Y. A.; Aladinskaya, A. V.; Veselov, M. S.; Aladinskiy, V. A.; Beloglazkina, E. K.; Koteliansky, V. E.; Shakhbazyan, A. G.; Sandulenko, Y. B.; Majouga, A. G. Small-Molecule PSMA Ligands. Current State, SAR and Perspectives. *Journal of Drug Targeting* **2016**, *24* (8), 679–693. https://doi.org/10.3109/1061186X.2016.1154564.
(23) Edelman, R. R. The History of MR Imaging as Seen through the Pages of Radiology. *Radiology* **2014**, *273* (2S), S181–S200. https://doi.org/10.1148/radiol.14140706.
(24) *The history of magnetic resonance imaging (MRI) | Royal Brompton & Harefield NHS Foundation Trust*. https://www.rbht.nhs.uk/blog/history-magnetic-resonance-imaging-mri (accessed 2020-10-19).
(25) Li, H.; Meade, T. J. Molecular Magnetic Resonance Imaging with Gd(III)-Based Contrast Agents: Challenges and Key Advances. *J. Am. Chem. Soc.* **2019**, *141* (43), 17025–17041. https://doi.org/10.1021/jacs.9b09149.
(26) Ballinger, J. R. *MRI physics | Radiology Reference Article | Radiopaedia.org*. Radiopaedia. https://radiopaedia.org/articles/mri-physics?lang=us (accessed 2020-02-26).
(27) Caravan, P. Strategies for Increasing the Sensitivity of Gadolinium Based MRI Contrast Agents. *Chem. Soc. Rev.* **2006**, *35* (6), 512–523. https://doi.org/10.1039/B510982P.
(28) Dale, B. M.; Brown, M. A.; Semelka, R. C. *MRI: Basic Principles and Applications*; John Wiley & Sons, Incorporated: New York, UNITED KINGDOM, 2015.
(29) Hornak, J. P. *The Basics of MRI*. https://www.cis.rit.edu/htbooks/mri/ (accessed 2020-03-02).
(30) Ibrahim, M. A.; Hazhirkarzar, B.; Dublin, A. B. Magnetic Resonance Imaging (MRI) Gadolinium. In *StatPearls*; StatPearls Publishing: Treasure Island (FL), 2020.
(31) MRI: The Dance of the Whirling Protons – The Alcohol Pharmacology Education Partnership.
(32) Xu, H.; Othman, S. F.; Magin, R. L. Monitoring Tissue Engineering Using Magnetic Resonance Imaging. *Journal of Bioscience and Bioengineering* **2008**, *106* (6), 515–527. https://doi.org/10.1263/jbb.106.515.
(33) Kurzhunov, D. Novel Reconstruction and Quantification Methods for Oxygen-17 Magnetic Resonance Imaging at Clinical Field Strengths. **2017**.
(34) *MRI: A Guided Tour - MagLab*. https://nationalmaglab.org/education/magnet-academy/learn-the-basics/stories/mri-a-guided-tour (accessed 2022-08-25).
(35) Boros, E.; Polasek, M.; Zhang, Z.; Caravan, P. Gd(DOTAla): A Single Amino Acid Gd-Complex as a Modular Tool for High Relaxivity MR Contrast Agent Development. *J. Am. Chem. Soc.* **2012**, *134* (48), 19858–19868. https://doi.org/10.1021/ja309187m.
(36) Helm, L. Optimization of Gadolinium-Based MRI Contrast Agents for High Magnetic-Field Applications. *Future Med Chem* **2010**, *2* (3), 385–396. https://doi.org/10.4155/fmc.09.174.
(37) Werner, E. J.; Datta, A.; Jocher, C. J.; Raymond, K. N. High-Relaxivity MRI Contrast Agents: Where Coordination Chemistry Meets Medical Imaging. *Angewandte Chemie International Edition 47*, 8568–8580.
(38) Yokoyama, M.; Shiraishi, K. Stability Evaluation of Gd Chelates for Macromolecular MRI Contrast Agents. *Magn Reson Mater Phy* **2020**, *33* (4), 527–536. https://doi.org/10.1007/s10334-019-00805-8.
(39) Hall, A. J.; Robertson, A. G.; Hill, L. R.; Rendina, L. M. Synthesis and Tumour Cell Uptake Studies of Gadolinium(III)–Phosphonium Complexes. *Sci Rep* **2021**, *11* (1), 598. https://doi.org/10.1038/s41598-020-79893-9.

(40) Ibrahim, M. A.; Hazhirkarzar, B.; Dublin, A. B. Gadolinium Magnetic Resonance Imaging. In *StatPearls*; StatPearls Publishing: Treasure Island (FL), 2022.
(41) Bower, D. V.; Richter, J. K.; von Tengg-Kobligk, H.; Heverhagen, J. T.; Runge, V. M. Gadolinium-Based MRI Contrast Agents Induce Mitochondrial Toxicity and Cell Death in Human Neurons, and Toxicity Increases With Reduced Kinetic Stability of the Agent. *Investigative Radiology* **2019**, *54* (8), 453–463. https://doi.org/10.1097/RLI.0000000000000567.
(42) Schmitthenner, H. F.; Dobson, D. E.; Jones, K. G.; Akporji, N.; Soika, D. Q. M.; Nastiuk, K. L.; Hornak, J. P. Modular Synthesis of DOTA-Metal-Based PSMA-Targeted Imaging Agents for MRI and PET of Prostate Cancer. *Chemistry* **2019**. https://doi.org/10.1002/chem.201903390.
(43) Azhdarinia, A.; Wilganowski, N.; Robinson, H.; Ghosh, P.; Kwon, S.; Lazard, Z. W.; Davis, A. R.; Olmsted-Davis, E.; Sevick-Muraca, E. M. Characterization of Chemical, Radiochemical and Optical Properties of a Dual-Labeled MMP-9 Targeting Peptide. *Bioorganic & Medicinal Chemistry* **2011**, *19* (12), 3769–3776. https://doi.org/10.1016/j.bmc.2011.04.054.
(44) Schmitthenner, H. F.; Barrett, T. M.; Beach, S. A.; Heese, L. E.; Weidman, C.; Dobson, D. E.; Mahoney, E. R.; Schug, N. C.; Jones, K. G.; Durmaz, C.; Otasowie, O.; Aronow, S.; Lee, Y. P.; Ophardt, H. D.; Becker, A. E.; Hornak, J. P.; Evans, I. M.; Ferran, M. C. Modular Synthesis of Peptide-Based Single- and Multimodal Targeted Molecular Imaging Agents. *ACS Appl. Bio Mater.* **2021**, *4* (7), 5435–5448. https://doi.org/10.1021/acsabm.1c00157.
(45) *Modular imaging agents containing amino acids and peptides - Patent EP-3027228-A4 - PubChem*. https://pubchem.ncbi.nlm.nih.gov/patent/EP-3027228-A4 (accessed 2022-08-06).
(46) Schmitthenner, H. F.; Sweeney-Jones, A. M.; Williams, S. Transmetalation Methods for the Synthesis of PET and SPECT Imaging Agents. US20160251378A1, September 1, 2016.
(47) López, S. E.; Salazar, J. Trifluoroacetic Acid: Uses and Recent Applications in Organic Synthesis. *Journal of Fluorine Chemistry* **2013**, *156*, 73–100. https://doi.org/10.1016/j.jfluchem.2013.09.004.
(48) Chen, Y.; Zhu, Q.; Tian, Y.; Tang, W.; Pan, F.; Xiong, R.; Yuan, Y.; Hu, A. Supramolecular Aggregates from Polyacrylates and Gd(III)-Containing Cationic Surfactants as High-Relaxivity MRI Contrast Agents. *Polym. Chem.* **2015**, *6* (9), 1521–1526. https://doi.org/10.1039/C4PY01562B.